

Fig. 4.13 Convergence curves for the free hyperboloid shell problem. The bold line represents the optimal convergence rate.

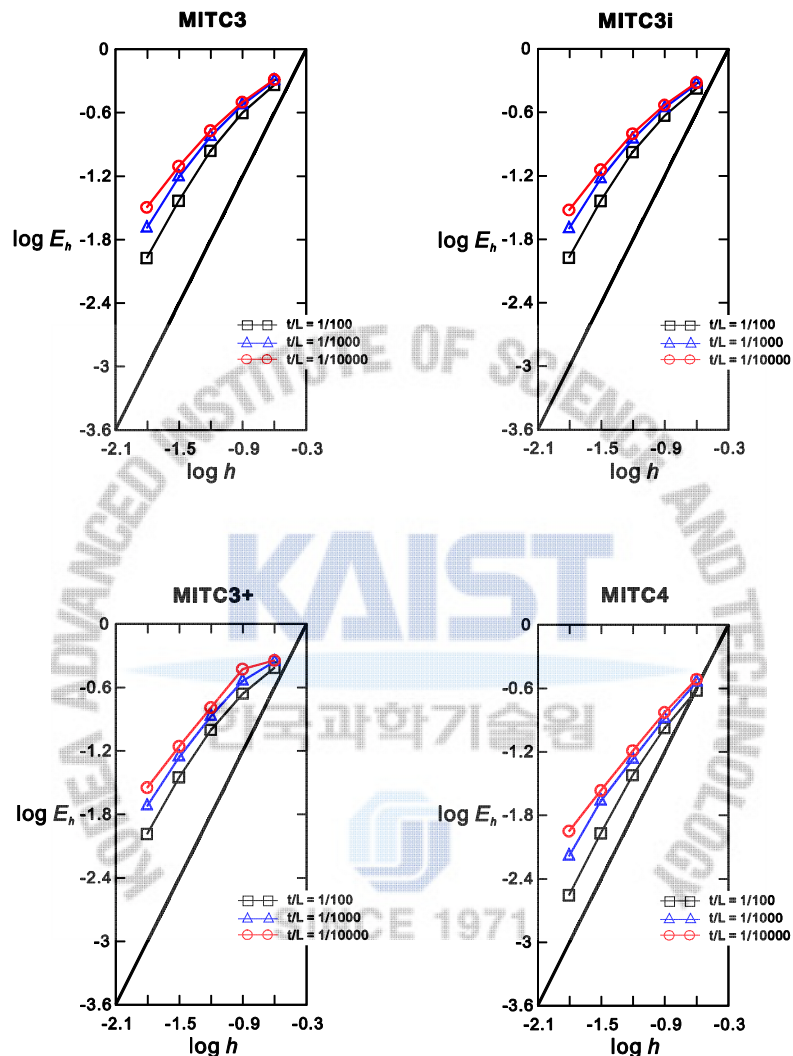


Fig. 4.14 Convergence curves for the clamped hyperboloid shell problem with the distorted meshes shown in Fig. 3.14. The bold line represents the optimal convergence rate.

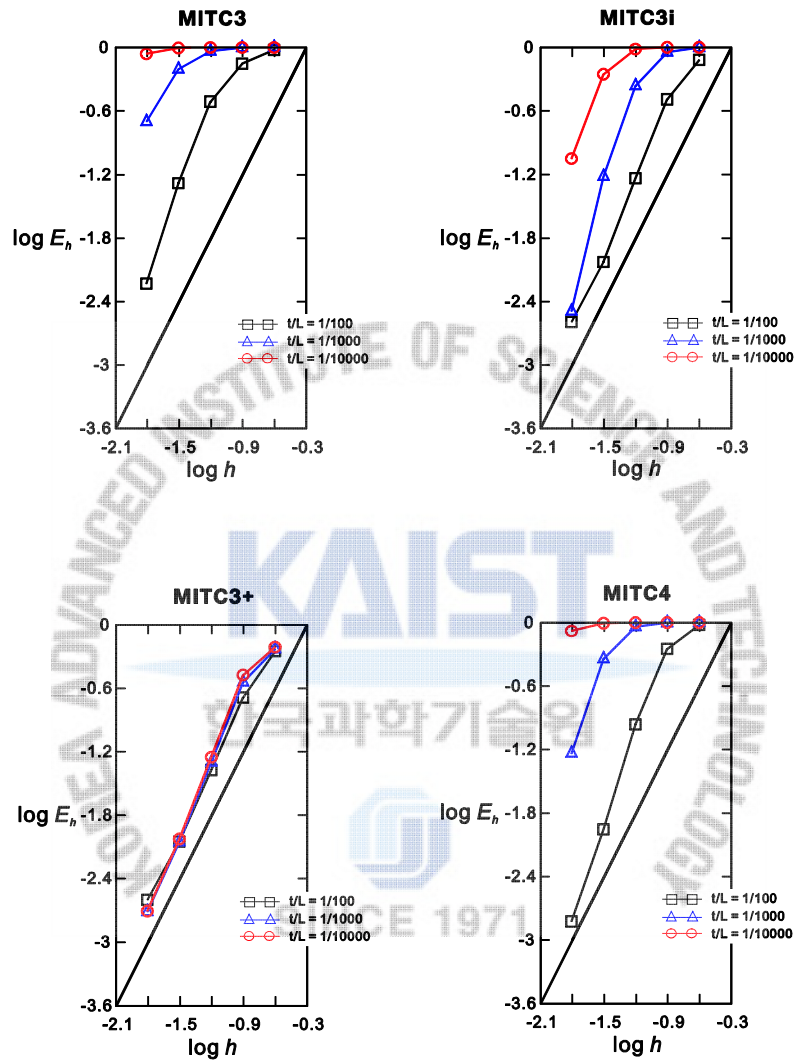


Fig. 4.15 Convergence curves for the free hyperboloid shell problem with the distorted meshes shown in Fig. 3.14. The bold line represents the optimal convergence rate.

Figs. 4.12 and 4.13 show the convergence curves for the clamped and free hyperboloid shell problems. In the clamped hyperboloid shell case, the performance of all four shell elements is similarly good. However, in the free hyperboloid shell case, the MITC3+ shell element shows much better convergence behavior compared to the other triangular shell elements.

Figs. 4.14 and 4.15 give the convergence curves of the MITC3, MITC3i, MITC3+ and MITC4 shell elements when the distorted meshes in Fig. 3.14 are used. The MITC3+ shell element still displays again an excellent convergence behavior even though the others present the deteriorated convergence behavior due to locking.

Note that, in all of the numerical studies presented in Sections 4.3 and 4.4, the standard 7-point Gauss integration in the r-s plane is employed to calculate the element stiffness matrix of the MITC3+ shell element due to the cubic bubble function. If the 3-point Gauss integration is used for the MITC3+ shell element, all of the basic numerical tests are also passed and similar convergence behaviors are observed. In the Ref. [54], considering a geometric nonlinear analysis using the total Lagrangian formulation and allowing for large displacements and large rotations, the excellent performance of the MITC3+ shell element is measured in the problems considered as performed in the linear analysis.

#### 4.5 Closure

The 3-node MITC3+ triangular shell element based on the ‘basic mathematical shell model’ is developed. A cubic bubble function for the rotations is used. A new assumed transverse shear strains field is constructed with a new tying scheme to reduce shear locking while satisfying the consistency and ellipticity conditions. For comparison, the shell element using the standard displacement interpolation of the 3-node shell element and the new assumed transverse shear strain field is considered.

The developed shell elements pass the basic numerical tests (the isotropy, zero energy mode, and patch tests) and the MITC3+ shell element shows an excellent convergence behavior in basic and encompassing convergence tests.

## Chapter 5.Modal behavior of the MITC3+ shell finite element

The MITC3+ shell element passes the three basic tests (the patch, zero energy mode and isotropy tests) and shows excellent convergence behaviors in various shell problems even when highly distorted meshes are used [24]. An excellent performance of the MITC3+ shell element in geometric nonlinear analysis was also measured [54]. With such encouraging results at hand, it is clearly of interest to further study this element and identify more deeply its fundamental features.

The objective in this chapter is to present a deeper understanding of the MITC3+ shell element through detailed static and dynamic mode solutions. The DISP3, MITC3 and MITC4 shell elements are also considered for comparisons. In the static mode solutions of a single right-angled triangular element and an assemblage of two right-angled triangular elements, we investigate the transverse shear strain fields in the bending modes. This study shows how the MITC3+ shell element performs on the mode level. The transverse shear strain fields of the MITC3+ shell element are also studied analytically in a two-sided clamped plate problem, to see whether and how locking occurs. In the dynamic mode solutions, the frequencies and mode shapes are evaluated considering a free square plate problem and a hyperboloid shell problem and the convergence of the frequencies is presented.

In the following sections, we first review the isotropic 3-node triangular shell finite elements. We then perform the static mode analyses for the tested elements. Next, we study the transverse shear strain fields of the MITC3+ shell element in the two-sided clamped plate problem. We also perform the dynamic mode analyses in completely free plate and shell problems.

### 5.1 Formulations of 3-node triangular shell elements

In this section, the formulations of the isotropic 3-node continuum mechanics based triangular shell finite elements are briefly reviewed: the DISP3, MITC3 and MITC3+ shell elements.

### 5.1.1 The DISP3 shell element

The geometry of a standard 3-node continuum mechanics based triangular shell finite element is obtained by [1,11]

$$\vec{x}(r,s,t) = \sum_{i=1}^3 h_i(r,s) \vec{x}_i + \frac{t}{2} \sum_{i=1}^3 a_i h_i(r,s) \vec{V}_n^i \quad \text{with } h_1 = 1 - r - s, \quad h_2 = r, \quad h_3 = s, \quad (5.1)$$

where  $h_i(r,s)$  is the two-dimensional interpolation function of the standard isoparametric procedure corresponding to node  $i$ ,  $\vec{x}_i$  is the position vector of node  $i$  in the global Cartesian coordinate system, and  $a_i$  and  $\vec{V}_n^i$  denote the shell thickness and the director vector at the node, see Fig. 3.1.

The corresponding displacement interpolation of the element is given by

$$\vec{u}(r,s,t) = \sum_{i=1}^3 h_i(r,s) \vec{u}_i + \frac{t}{2} \sum_{i=1}^3 a_i h_i(r,s) (-\vec{V}_2^i \alpha_i + \vec{V}_1^i \beta_i), \quad (5.2)$$

in which  $\vec{u}_i$  is the nodal displacement vector in the global Cartesian coordinate system,  $\vec{V}_1^i$  and  $\vec{V}_2^i$  are unit vectors orthogonal to  $\vec{V}_n^i$  and to each other, and  $\alpha_i$  and  $\beta_i$  are the rotations of the director vector  $\vec{V}_n^i$  about  $\vec{V}_1^i$  and  $\vec{V}_2^i$ , respectively, at node  $i$ .

The linear part of the displacement-based covariant strain components is given by

$$e_{ij} = \frac{1}{2} (\vec{g}_i \cdot \vec{u}_j + \vec{g}_j \cdot \vec{u}_i), \quad (5.3)$$

in which

$$\vec{g}_i = \frac{\partial \vec{x}}{\partial r_i}, \quad \vec{u}_i = \frac{\partial \vec{u}}{\partial r_i} \quad \text{with } r_1 = r, \quad r_2 = s, \quad r_3 = t, \quad (5.4)$$

The displacement-based 3-node shell finite element has no spurious zero energy mode and satisfies the isotropy condition. However, in the bending-dominated problems, this shell finite element is extremely stiff due to locking [11].

### 5.1.2 The MITC3 shell element

The geometry and displacement interpolations are identical to the DISP3 shell element, but the MITC

method is applied [1]. The covariant in-plane strain components are obtained by Eq. (5.3) because the geometry of the 3-node triangular shell finite element is flat. The MITC method is only applied to construct the covariant transverse shear strain field with constant covariant transverse shear strain conditions along the edges. The assumed transverse shear strain field of the MITC3 shell element is given by [10]

$$\tilde{e}_{rt}^{MITC3} = e_{rt}^{(1)} + cs, \quad \tilde{e}_{st}^{MITC3} = e_{st}^{(2)} - cr, \quad (5.5)$$

in which  $c = (e_{rt}^{(3)} - e_{rt}^{(1)}) - (e_{st}^{(3)} - e_{st}^{(2)})$  and the tying points are shown in Fig. 3.3.

The MITC3 shell element passes the basic tests: zero energy mode, isotropy and patch tests. In convergence tests, the practically good convergence behavior is presented. However, when the thickness decreases, some locking occurs in bending-dominated problems [10].

### 5.1.3 The MITC3+ shell element

The geometry of the MITC3+ shell element, see Fig. 4.1, is interpolated by

$$\vec{x}(r,s,t) = \sum_{i=1}^3 h_i(r,s) \vec{x}_i + \frac{t}{2} \sum_{i=1}^4 a_i f_i(r,s) \vec{V}_n^i \quad \text{with} \quad a_4 \vec{V}_n^4 = \frac{1}{3} (a_1 \vec{V}_n^1 + a_2 \vec{V}_n^2 + a_3 \vec{V}_n^3), \quad (5.6)$$

in which the  $f_i(r,s)$  are two-dimensional interpolation functions with the cubic bubble function  $f_4$  corresponding to the internal node 4

$$f_1 = h_1 - \frac{1}{3} f_4, \quad f_2 = h_2 - \frac{1}{3} f_4, \quad f_3 = h_3 - \frac{1}{3} f_4, \quad f_4 = 27rs(1-r-s). \quad (5.7)$$

From Eq. (5.6), the displacement interpolation is described by

$$\vec{u}(r,s,t) = \sum_{i=1}^3 h_i(r,s) \vec{u}_i + \frac{t}{2} \sum_{i=1}^4 a_i f_i(r,s) (-\vec{V}_2^i \alpha_i + \vec{V}_1^i \beta_i), \quad (5.8)$$

where  $\alpha_4$  and  $\beta_4$  are the rotation degrees of freedom at the bubble node [24].

Since the bubble node that includes only rotation degree of freedom is positioned at the average of the three corner nodes of the element, the geometry of the MITC3+ shell element is also flat. Hence, the transverse shear strain components are only established using the MITC method.

The assumed transverse shear strain field of the MITC3+ shell finite element is given by [24]

$$\begin{aligned}\hat{e}_{rt}^{MITC3+} &= \frac{2}{3}(e_{rt}^{(B)} - \frac{1}{2}e_{st}^{(B)}) + \frac{1}{3}(e_{rt}^{(C)} + e_{st}^{(C)}) + \frac{1}{3}\hat{c}(3s-1), \\ \hat{e}_{st}^{MITC3+} &= \frac{2}{3}(e_{st}^{(A)} - \frac{1}{2}e_{rt}^{(A)}) + \frac{1}{3}(e_{rt}^{(C)} + e_{st}^{(C)}) + \frac{1}{3}\hat{c}(1-3r),\end{aligned}\quad (5.9)$$

in which  $\hat{c} = (e_{rt}^{(F)} - e_{rt}^{(D)}) - (e_{st}^{(F)} - e_{st}^{(E)})$  and the 6 tying points (A)-(F) with the tying distance  $d$  defined for the tying points (D)-(F) are presented in Fig. 4.3 and Table 4.1. A fixed value  $d = 1/10,000$  is suggested in Ref. [24].

The MITC3+ shell element passes the basic tests: zero energy mode, isotropy and patch tests. The excellent convergence behavior is reported considering various thickness and element distortions [24].

## 5.2 Static mode analysis

In this section, we perform the static mode solutions of the DISP3, MITC3 and MITC3+ shell elements considering two plate bending cases: a single right-angled triangular shell element and an assemblage of two right-angled triangular shell elements. Note that membrane locking is not present because the geometry of the 3-node triangular shell elements is flat.

For the static mode solution, the following eigenvalue problem is considered

$$\mathbf{K}\vec{\phi}_i^s = \lambda_i^s \vec{\phi}_i^s \quad \text{with } i = 1, 2, \dots, N, \quad (5.10)$$

where  $\mathbf{K}$  is the stiffness matrix,  $\lambda_i^s$  and  $\vec{\phi}_i^s$  are the eigenvalue and orthonormal eigenvector of the  $i$ th static mode, respectively, and  $N$  is the number of degrees of freedom [1]. The eigenvector represents a deformation mode and the corresponding eigenvalue is twice of the strain energy stored in that deformation, since  $\vec{\phi}_i^s T \vec{\phi}_i^s = 1$ .

For the deformation mode  $\vec{\phi}_i^s$ , the strain fields defined in the global Cartesian coordinate are

$$\vec{\varepsilon} = \mathbf{B}\vec{\phi}_i^s \quad \text{with} \quad \vec{\varepsilon} = [\varepsilon_{xx} \quad \varepsilon_{yy} \quad \gamma_{xy} \quad \gamma_{xz} \quad \gamma_{yz}]^T, \quad (5.11)$$

where  $\mathbf{B}$  is the strain-displacement relation matrix obtained in the finite element formulation.

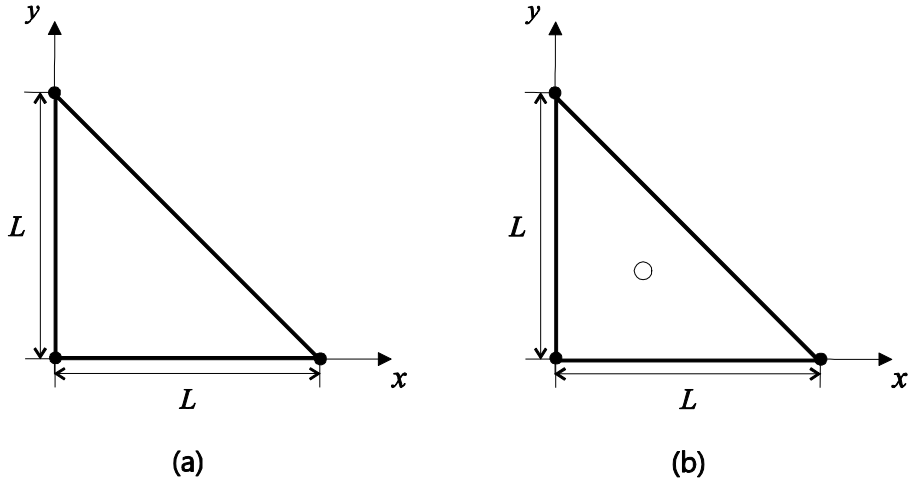


Fig. 5.1 A single right-angled triangular shell element for plate bending problem ( $L=1.0$ ,  $a/L=1/10,000$ ,  $E=1.7472\times 10^7$  and  $\nu=0.3$ ). (a) A single 3-node triangular shell element. (b) A single 3-node triangular shell element with the bubble node on rotations.

Using the above relations, we can study the detailed strain behavior of shell finite elements in each eigenvector mode. Since shell finite elements should produce zero transverse shear strains in the bending modes, important insight into shear locking of an element can be obtained when considering the eigenvectors.

### 5.2.1 Single right-angled triangular element

As shown in Fig. 5.1, we consider a single right-angled triangular shell element with free boundary (length  $L=1.0$ , thickness to length ratio  $a/L=1/10,000$ , Young's modulus  $E=1.7472\times 10^7$  and Poisson's ratio  $\nu=0.3$ ). The static mode solutions are performed for the DISP3, MITC3 and MITC3+ shell finite elements, and we focus on the static modes related to plate bending.

The eigenvalues of the stiffness matrices of the DISP3, MITC3 and MITC3+ shell elements are presented in Table 5.1. The modes are named based on their fundamental kinematics (bending, in-plane twisting, transverse shearing, and membrane kinematics). While the DISP3 and MITC3 shell elements have the 3 symmetric bending modes B1, B2, and B3 shown in Fig. 5.2, the MITC3+ shell element has 2 additional

antisymmetric bending modes  $B1+$  and  $B2+$  shown in Fig. 5.3(a) and (b) due to the bubble function enrichment on rotations. Note that the antisymmetric bending modes  $B1+$  and  $B2+$  "correspond" to the symmetric bending modes  $B1$  and  $B3$ , respectively. It is observed that, in the bending modes  $B1$ ,  $B2$  and  $B3$ , the eigenvalues of the DISP3 shell element are much larger than those of the MITC3 and MITC3+ shell element. That is, the DISP3 shell element is much stiffer. Another important observation is that the MITC3+ shell element contains a much more flexible in-plane twisting mode T than the MITC3 shell element.

Next, on the deformation mode level, the transverse shearing behavior of the DISP3, MITC3 and MITC3+ shell elements is investigated. The bending modes  $B1$ ,  $B2$ ,  $B3$ ,  $B1+$  and  $B2+$  are considered. Note that the transverse shear strains should be zero in the bending modes. Table 5.2 summarizes the strain fields of the DISP3 and MITC3 shell elements obtained by Eq. (5.11) in the bending modes. Obviously, the DISP3 shell element produces non-zero transverse shear strains in all bending modes, that is, the element severely locks.

However, the MITC3 shell element produces zero transverse shear strains in the bending modes  $B1$ ,  $B2$  and  $B3$ . Hence the shear locking is completely removed on the element level. A further analysis shows that the same observation holds for a single MITC3 triangular element of arbitrary shape. However, it is important to note that, nevertheless, the MITC3 shell element still shows shear locking on the element assemblage level, see the convergence test results in Refs. [10, 11, 12, 24]. Of course, the locking is much less severe than for the DISP3 shell element.

The MITC3+ shell element also gives zero transverse shears in the bending modes  $B1$ ,  $B2$  and  $B3$ . In addition, Table 5.3 presents the strain fields in the bending modes  $B1+$  and  $B2+$  and shows that in these bending modes, as well, zero transverse shear strains are seen.

We also investigate the strain fields of the MITC3+ shell element in the in-plane twisting mode T shown in Fig. 5.3(c). Table 5.3 shows that the transverse shear strains in the in-plane twisting mode depend on the tying distance  $d$  defined in Fig. 4.3(c) and Table 4.1. In Refs. [12, 24], we observed that the performance of the 3-node shell element can be improved by reducing the transverse shear strains in the in-plane twisting mode. In the following section, we study how the in-plane twisting mode affects the modal behavior.

Table 5.1 Eigenvalues of the stiffness matrices of the single triangular shell element for the element geometry shown in Fig. 5.1. Note that modes 1 to 6 produce zero eigenvalues corresponding to rigid body modes. The order of zero eigenvalues calculated is smaller than 1.0E-12.

Mode	DISP3		MITC3		MITC3+	
7	<u>2.8000E+01</u>	T	<u>6.6764E-07</u>	B1	<u>6.6685E-07</u>	B1
8	<u>2.8000E+01</u>	B1	<u>8.1455E-07</u>	B2	<u>7.9621E-07</u>	B2
9	<u>2.8000E+01</u>	B2	<u>2.4924E-06</u>	B3	<u>2.4921E-06</u>	B3
10	<u>2.8000E+01</u>	B3	<u>3.6928E+01</u>	T	<u>8.3107E-06</u>	B1+
11	4.4800E+02	S1	4.6707E+02	S1	<u>1.3599E-05</u>	T
12	8.3813E+02	M	8.3813E+02	M	<u>1.4128E-05</u>	B2+
13	1.1200E+03	S2	1.1760E+03	S2	4.6667E+02	S1
14	1.3440E+03	M	1.3440E+03	M	8.3813E+02	M
15	3.0019E+03	M	3.0019E+03	M	1.1760E+03	S2
16	-		-		1.3440E+03	M
17	-		-		3.0019E+03	M

B: Bending modes, T: In-plane twisting mode, S: Transverse shearing modes, M: Membrane modes, B+: Bending modes due to the bubble function enrichment

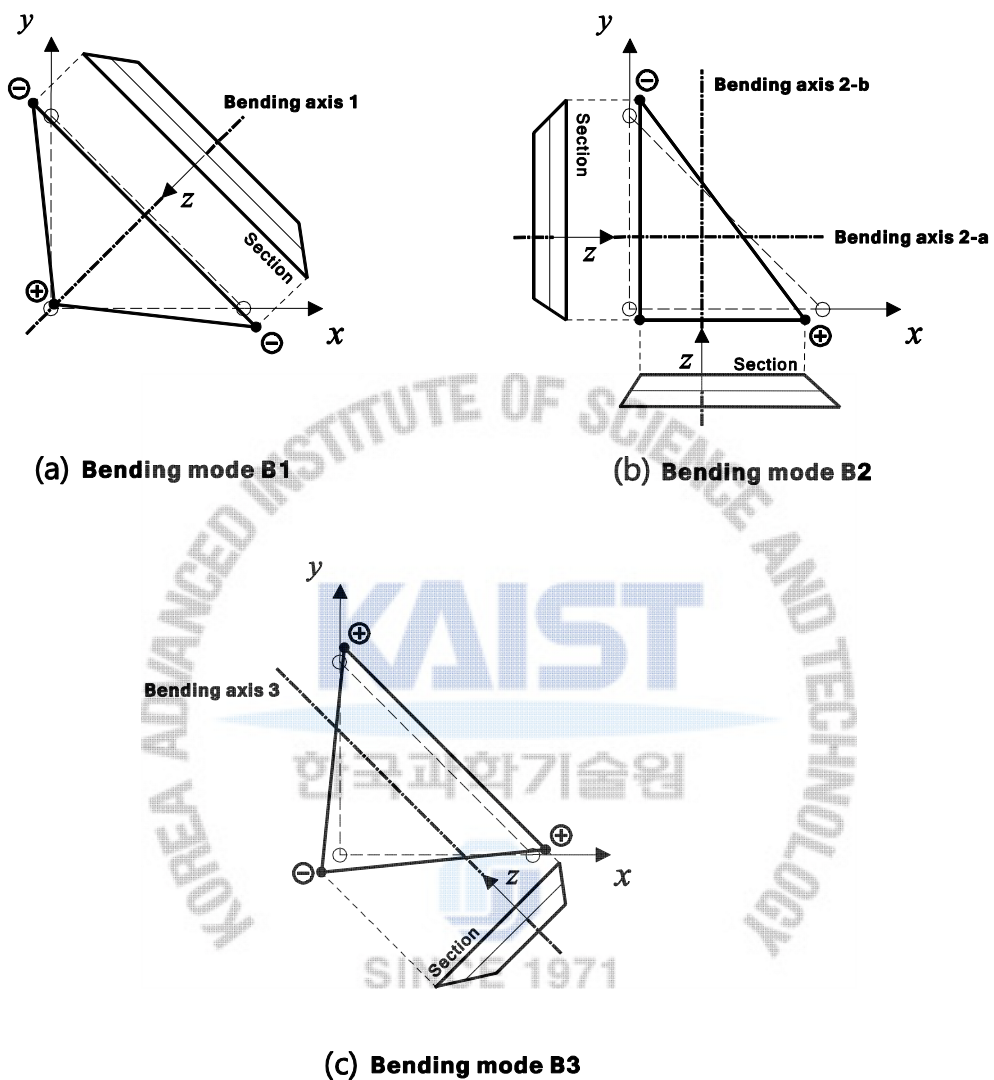


Fig. 5.2 Shapes of the bending modes for the single right-angled MITC3 shell element shown in Fig. 5.1(a). The dotted and solid lines correspond to the top surfaces before and after deformation, respectively, on the  $xy$ -plane. Plus and minus signs denote small out-of-plane displacements in the  $z$  and  $-z$  directions, respectively.

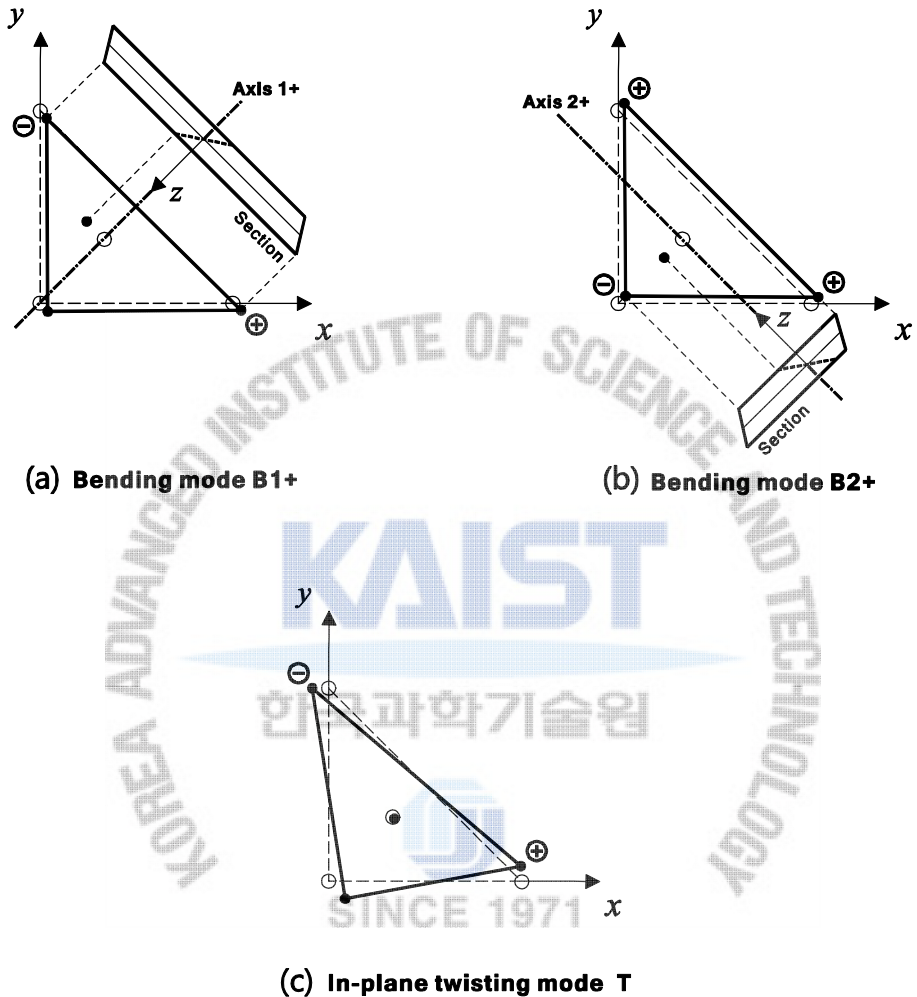


Fig. 5.3 Mode shapes of the single right-angled MITC3+ shell element shown in Fig. 5.1(b). The dotted and solid lines correspond to the top surfaces before and after deformation, respectively, on the  $xy$ -plane. Plus and minus signs denote small out-of-plane displacements in the  $z$  and  $-z$  directions, respectively.

Table 5.2 Strain fields of the single right-angled DISP3 and MITC3 shell elements in the bending modes B1, B2 and B3.

$$a/L = 0.0001, z = a(t/2)$$

Bending mode		DISP3	MITC3
B1	Eigenvalue	2.8000E+01	6.6764E-07
	Bending Strains	$\varepsilon_{xx} = 0.280z$ $\varepsilon_{yy} = 0.280z$ $\gamma_{xy} = -1.38z$	$\varepsilon_{xx} = 0.269z$ $\varepsilon_{yy} = 0.269z$ $\gamma_{xy} = -1.36z$
	Transverse shear strains	$\gamma_{xz} = 0.137 + 0.280r - 0.691s$ $\gamma_{yz} = 0.137 - 0.691r + 0.280s$	$\gamma_{xz} = 0.0$ $\gamma_{yz} = 0.0$
B2	Eigenvalue	2.8000E+01	8.1455E-07
	Bending Strains	$\varepsilon_{xx} = -z$ $\varepsilon_{yy} = z$ $\gamma_{xy} = 0.0$	$\varepsilon_{xx} = -0.853z$ $\varepsilon_{yy} = 0.853z$ $\gamma_{xy} = 0.0$
	Transverse shear strains	$\gamma_{xz} = 0.5 - r - 0.5s$ $\gamma_{yz} = -0.5 + 0.5r + s$	$\gamma_{xz} = 0.0$ $\gamma_{yz} = 0.0$
B3	Eigenvalue	2.8000E+01	2.4924E-06
	Bending strains	$\varepsilon_{xx} = 0.960z$ $\varepsilon_{yy} = 0.960z$ $\gamma_{xy} = 1.45z$	$\varepsilon_{xx} = 0.963z$ $\varepsilon_{yy} = 0.963z$ $\gamma_{xy} = -1.42z$
	Transverse shear strains	$\gamma_{xz} = -0.561 + 0.960r + 0.723s$ $\gamma_{yz} = -0.561 + 0.723r + 0.960s$	$\gamma_{xz} = 0.0$ $\gamma_{yz} = 0.0$

Table 5.3 Strain fields of the single right-angled MITC3+shell element in the bending modes B1+ and B2+, and in-plane twisting mode T.

$$a/L = 0.0001, z = a(t/2)$$

Bending mode B1+	Eigenvalue	8.3107E-06
	Bending strains	$\varepsilon_{xx} = [0.019 - 21.3(s-2rs-s^2)]z$ $\varepsilon_{yy} = [-0.019 + 21.3(r-2rs-r^2)]z$ $\gamma_{xy} = -21.3(r-s-r^2+s^2)z$
	Transverse shear strains	$\gamma_{xz} = 0.0$ $\gamma_{yz} = 0.0$
Bending mode B2+	Eigenvalue	1.4128E-05
	Bending strains	$\varepsilon_{xx} = [-0.001 - 21.8(s-2rs-s^2)]z$ $\varepsilon_{yy} = [-0.001 - 21.8(r-2rs-r^2)]z$ $\gamma_{xy} = [-0.064 - 21.8(r+s-4rs-r^2-s^2)]z$
	Transverse shear strains	$\gamma_{xz} = 0.0$ $\gamma_{yz} = 0.0$
In-plane twisting mode T ( $d = 1/10,000$ )	Eigenvalue	1.3599 E-05
	Bending strains	$\varepsilon_{xx} = [-0.514 + 1.49(s-2rs-s^2)]z$ $\varepsilon_{yy} = [0.514 - 1.49(r-2rs-r^2)]z$ $\gamma_{xy} = 1.49(r-s-r^2+s^2)z$
	Transverse shear strains	$\gamma_{xz} = 1.99d(1 - 3s)$ $\gamma_{yz} = 1.99d(-1 + 3r)$

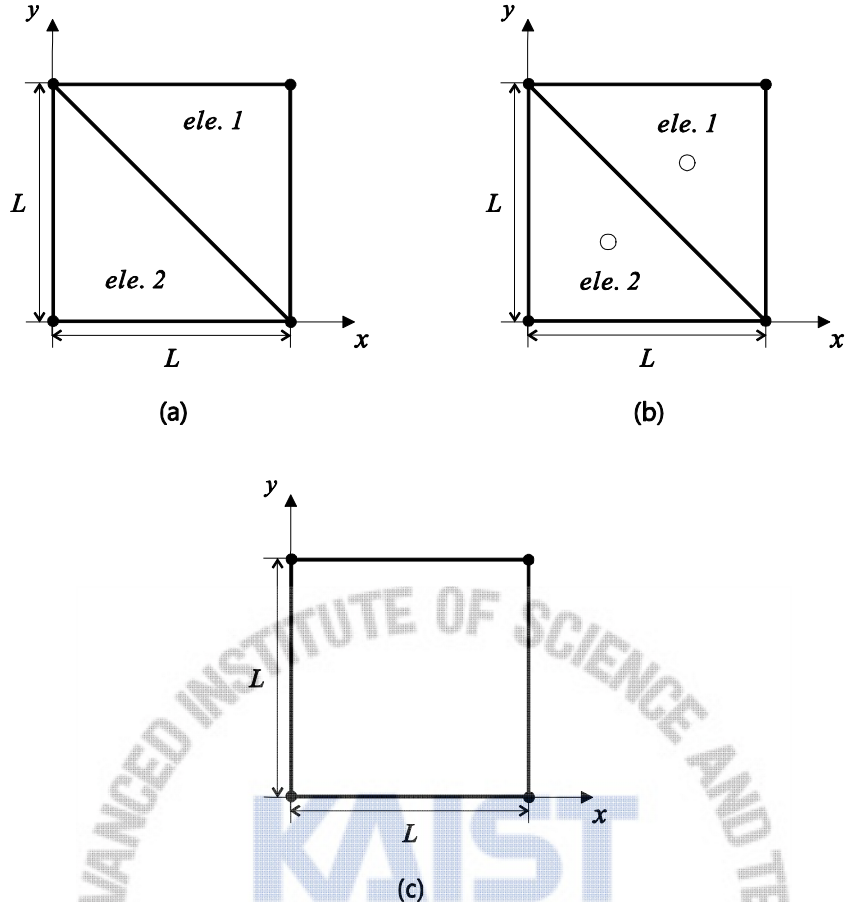


Fig. 5.4 An assemblage of two right-angled triangular elements ( $L=1.0$ ,  $E=1.7472 \times 10^7$  and  $\nu=0.3$ ). (a) Assemblage of two 3-node triangular shell elements. (b) Assemblage of two 3-node triangular shell elements with the bubble nodes on rotations.(c) A single 4-node quadrilateral shell element.

### 5.2.2 Assemblage of two right-angled triangular elements

We consider an assemblage of two right-angled triangular shell elements with free boundary as shown in Figs. 5.4(a) and (b). The static mode solution is performed for the MITC3 and MITC3+ shell elements, and, for comparison, a single MITC4 shell element is also tested, see Fig. 5.4(c). We use  $a/L=1/10,000$  ,  $E=1.7472 \times 10^7$  and  $\nu=0.3$  .

Table 5.4 presents the eigenvalues of the stiffness matrices of the MITC4, MITC3 and MITC3+ models. The deformation modes are named based on their kinematics (bending, in-plane twisting, transverse shearing, and membrane kinematics). All shell element models produce 6 bending modes BC1, BC2, BC3, BC4, BL1 and BL2, and the MITC3+ shell element additionally produces 4 bending modes BQ1+, BQ2+, BQ3+ and BQ4+

due to the bubble function enrichment on rotations. It is seen that, in the bending mode BL1 shown in Fig. 5.5, the MITC3 shell element shows a much stiffer behavior than the MITC4 and MITC3+ shell elements. Compared to the MITC3 shell element, the MITC3+ shell element is much more flexible in the bending mode BL1 and in the in-plane twisting mode TQ.

In Ref. [24], we observed that, for a *single* MITC3+ shell element, as the tying distance  $d$  decreases, the eigenvalue corresponding to the in-plane twisting mode T decreases and is zero when  $d = 0$ . Considering now the assemblage of the MITC3+ shell elements shown in Fig. 5.4(b), we also perform the eigenvalue test by varying the tying distance  $d$ . Table 5.5 presents the eigenvalues of the assemblage of the two MITC3+ shell elements. As the tying distance  $d$  decreases (that is, the eigenvalue of the in-plane twisting mode T of a single MITC3+ element becomes smaller), the eigenvalues corresponding to the bending mode BL1 and in-plane twisting mode TQ decrease together. This fact implies that the in-plane twisting acts together with the bending mode BL1. In Table 5.5, we also show that, unlike for a single MITC3+ shell element [2], a zero eigenvalue is not present when  $d = 0$ . The reason is graphically explained in Fig. 5.6, which shows that the in-plane twisting mode of an assemblage of two triangular shell elements cannot be activated like for a single triangular shell element [24, 55].

Table 5.6 presents the strain fields for the MITC4, MITC3 and MITC3+ shell elements to investigate the shear locking behavior in the bending mode BL1. For the MITC4 shell element, the bending mode BL1 produces the linear bending strain fields for  $\varepsilon_{xx}$ ,  $\varepsilon_{yy}$  and  $\gamma_{xy}$  (that is, the strain fields are the linear functions of  $r$  and  $s$ ) and zero transverse shear strains. The bending mode BL1 of the MITC3 shell elements produces constant bending strain fields and non-zero transverse shear strains, that is, shear locking occurs in the element assemblage. However, with the help of the bending mode B1+ of a single MITC3+ shell element, in the bending mode BL1, the MITC3+ shell element produces bending strain fields up to quadratic order for  $\varepsilon_{xx}$ ,  $\varepsilon_{yy}$  and  $\gamma_{xy}$  and zero transverse shear strains when  $d = 0$ . Hence, in the bending mode BL1, shear locking can be alleviated with a small value of  $d$  and is completely removed with  $d = 0$ .

In summary, for the MITC3+ element, an enriched bending strain field is provided through the bending mode BL1 for the two element assemblage. The shear locking in this mode is alleviated by reducing the stiffness in the in-plane twisting mode T of a single MITC3+ shell element. This behavior is not present in the MITC3 shell element, which does not lock on the element level, but locks in the two element assemblage due to a deficiency of pure bending modes.

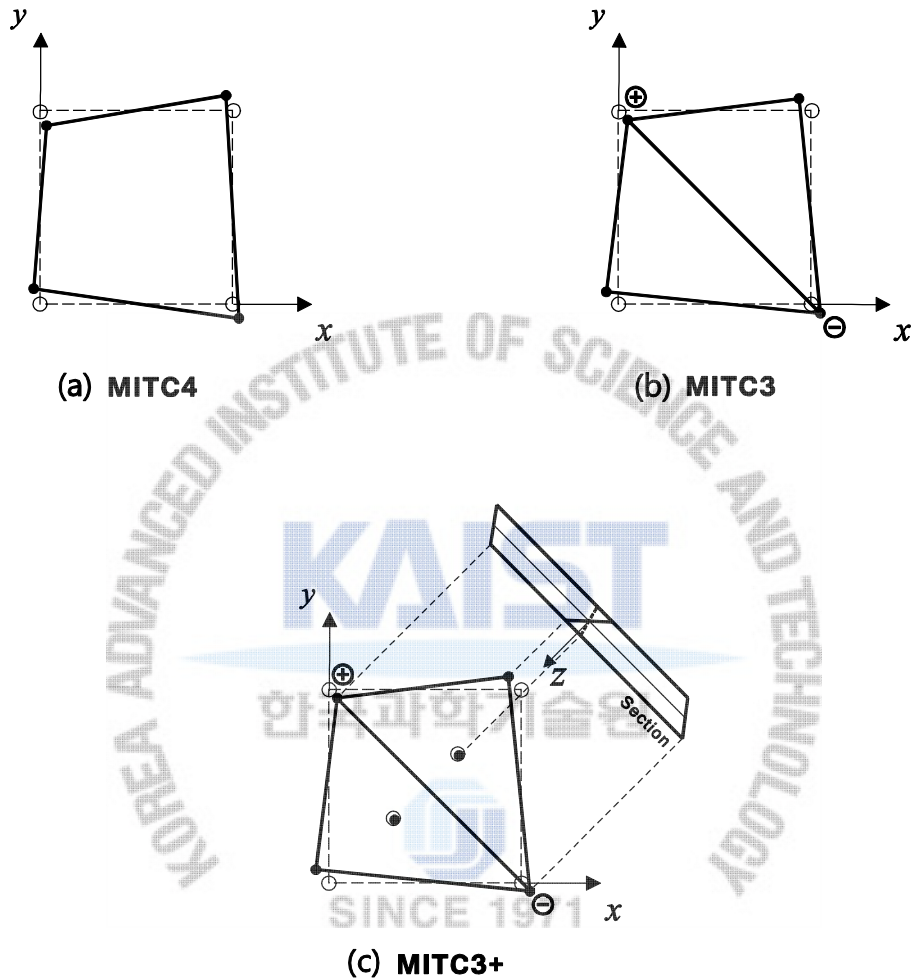


Fig. 5.5 Shapes of the bending mode BL1 shown in Fig. 5.4. The dotted and solid lines correspond to the top surfaces before and after deformation, respectively, on the  $xy$ -plane. Plus and minus signs denote small out-of-plane displacements in the  $z$  and  $-z$  directions, respectively.

Table 5.4 Eigenvalues of an assemblage of two right-angled triangular shell elements shown in Fig. 5.4 when  $a/L = 1/10,000$ . Note that modes 1 to 6 produce zero eigenvalues corresponding to rigid body modes. The order of zero eigenvalues calculated is smaller than 1.0E-12.

Mode	MITC4		MITC3		MITC3+	
7	<u>7.2000E-07</u>	BL1	<u>9.9556E-07</u>	BC1	<u>9.3805E-07</u>	BC1
8	<u>7.2000E-07</u>	BL2	<u>1.1200E-06</u>	BC2	<u>1.0608E-06</u>	BC2
9	<u>9.9556E-07</u>	BC1	<u>2.0800E-06</u>	BC3	<u>1.9629E-06</u>	BC3
10	<u>1.1200E-06</u>	BC2	<u>3.2000E-06</u>	BL2	<u>3.0544E-06</u>	BL2
11	<u>2.0800E-06</u>	BC3	<u>3.4167E+01</u>	BL1	<u>8.9316E-06</u>	BQ1+
12	<u>5.6000E+01</u>	TQ	<u>5.6000E+01</u>	TQ	<u>1.1912E-05</u>	BQ2+
13	<u>5.0400E+02</u>	BC4	<u>8.4000E+02</u>	SQ1	<u>1.4173E-05</u>	TQ
14	<u>8.4000E+02</u>	SQ1	<u>9.1783E+02</u>	SQ2	<u>1.5159E-05</u>	BL1
15	<u>8.4000E+02</u>	SQ2	<u>1.3440E+03</u>	MQ	<u>1.6660E-05</u>	BQ3+
16	<u>8.6400E+02</u>	MQ	<u>1.3440E+03</u>	MQ	<u>9.3333E+01</u>	BQ4+
17	<u>8.6400E+02</u>	MQ	<u>1.3440E+03</u>	MQ	<u>8.0267E+02</u>	SQ1
18	<u>1.3440E+03</u>	MQ	<u>1.5120E+03</u>	BC4	<u>8.4000E+02</u>	SQ2
19	<u>1.3440E+03</u>	MQ	<u>2.4960E+03</u>	MQ	<u>1.3440E+03</u>	MQ
20	<u>2.4960E+03</u>	MQ	<u>3.8400E+03</u>	MQ	<u>1.3440E+03</u>	MQ
21	-		-		<u>1.3440E+03</u>	MQ
22	-		-		<u>1.5493E+03</u>	BC4
23	-		-		<u>2.4960E+03</u>	MQ
24	-		-		<u>3.8400E+03</u>	MQ

BC: Bending modes with constant bending strain fields, BL: Bending modes with linear bending strain fields, TQ: In-plane twisting mode, SQ: Transverse shearing modes, MQ: Membrane modes, BQ+: Bending modes due to the bubble function enrichment

Table 5.5 Eigenvalues of the stiffness matrix of the assemblage of two MTC3+ shell elements shown in Fig. 5.4(b) according to the tying distance  $d$  in the plate bending problem when  $a/L = 1/10,000$ . Note that modes 1 to 6 produce zero eigenvalues corresponding to rigid body modes. The order of zero eigenvalues calculated is smaller than 1.0E-12. Modes 19-21, 23 and 24 are membrane modes. When  $d = 1/10,000$ , the eigenvalues are present in Table 5.4.

Mode	$d$	1/100	1/1,000	1/100,000	0.0		
7	9.3805E-07	BC1	9.3805E-07	BC1	9.3805E-07	BC1	9.3805E-07
8	1.0611E-06	BC2	1.0611E-06	BC2	1.0545E-06	BC2	<u>1.0099E-06</u>
9	1.9629E-06	BC3	1.9629E-06	BC3	<u>1.1303E-06</u>	BL1	1.0522E-06
10	3.0544E-06	BL2	3.0544E-06	BL2	<u>1.5394E-06</u>	TQ	<u>1.4140E-06</u>
11	9.7882E-06	BQ1+	9.7846E-06	BQ1+	1.9629E-06	BC3	1.9629E-06
12	1.1912E-05	BQ2+	1.1912E-05	BQ2+	3.0544E-06	BL2	3.0544E-06
13	1.6660E-05	BQ3+	1.6660E-05	BQ3+	1.0320E-05	BQ1+	1.0312E-05
14	<u>1.2767E-01</u>	TQ	<u>1.2782E-03</u>	TQ	1.1912E-05	BQ2+	1.1912E-05
15	<u>1.2768E-01</u>	BL1	<u>1.2783E-03</u>	BL1	1.6660E-05	BQ3+	1.6660E-05
16	9.3340E+01	BQ4+	9.3333E+01	BQ4+	9.3333E+01	BQ4+	9.3333E+01
17	8.0267E+02	SQ1	8.0267E+02	SQ1	8.0267E+02	SQ1	8.0267E+02
18	8.4001E+02	SQ2	8.4000E+02	SQ2	8.4000E+02	SQ2	8.4000E+02
22	1.5493E+03	BC4	1.5493E+03	BC4	1.5493E+03	BC4	1.5493E+03

BC: Bending modes with constant bending strain fields, BL: Bending modes with linear bending strain fields,

TQ: In-plane twisting mode, SQ: Transverse shearing modes, BQ+: Bending modes due to the bubble function enrichment

Table 5.6 Strain fields of the MITC4, MITC3 and MITC3+ shell element in the bending mode BL1.

$$a/L = 0.0001, z = a(t/2)$$

MITC4	MITC3 ( <i>ele. 1</i> )	MITC3+ ( <i>ele. 1, d = 0</i> )
Eig. : 7.2000E-07	Eig. : 3.4167E+01	Eig. : 1.0099E-06
$\varepsilon_{xx} = -0.403sz$	$\varepsilon_{xx} = -0.675z$	$\varepsilon_{xx} = [-0.670 - 0.401(s-2rs-s^2)]z$
$\varepsilon_{yy} = 0.915rz$	$\varepsilon_{yy} = 0.675z$	$\varepsilon_{yy} = [0.670 + 0.401(r-2rs-r^2)]z$
$\gamma_{xy} = (-0.403r + 0.915s)z$	$\gamma_{xy} = 0.0$	$\gamma_{xy} = 0.401(-r+s+r^2-s^2)z$
$\gamma_{xz} = 0.0$	$\gamma_{xz} = -0.235 + 0.675s$	$\gamma_{xz} = -1.34d(1 - 3s)$
$\gamma_{yz} = 0.0$	$\gamma_{yz} = 0.235 - 0.675r$	$\gamma_{yz} = -1.34d(-1 + 3r)$

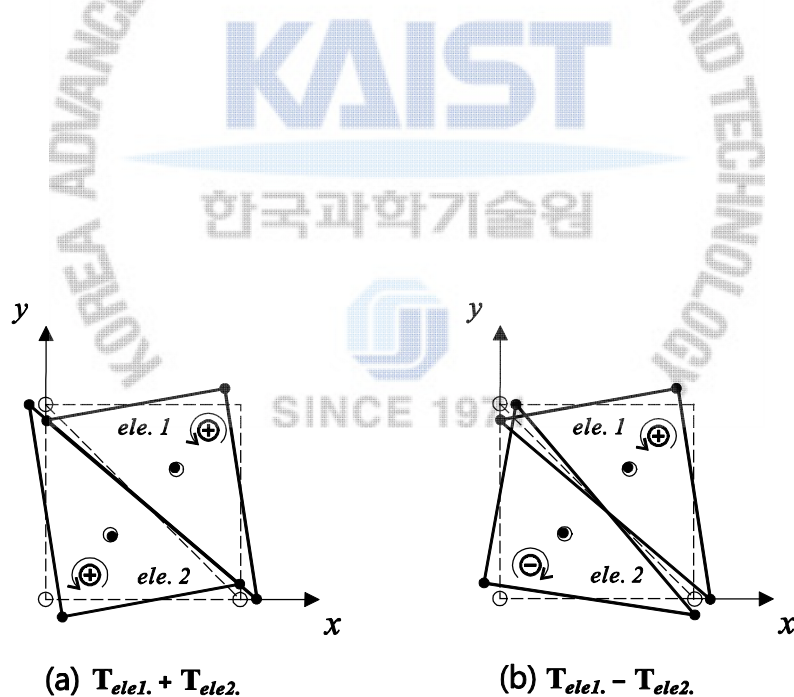


Fig. 5.6 In-plane twisting of two 3-node triangular shell elements. The dotted and solid lines correspond to the top surfaces before and after deformation, respectively, in the  $xy$ -plane.

### 5.3 Two-sided clamped plate problem

In this section, we study the behavior of the MITC3+ shell element in the two-sided clamped plate of dimension  $L \times L$  shown Fig. 5.7. This plate is subjected to uniform moments  $m_\alpha$  and  $-m_\beta$  along its free sides. The boundary conditions are  $u = v = w = \alpha = \beta = 0$  along the two clamped edges.

This plate problem was used to investigate the shear locking behavior of 3-node triangular shell elements in Ref. [11], which reports that, while the MITC3 shell element does not lock in Mesh B, the shell element severely locks in Mesh A. In general, triangular shell elements show such stiff behavior in Mesh A due to shear locking. To improve the performance of 3-node triangular shell elements, this phenomenon should be overcome. Hence, we investigate the effectiveness of the MITC3+ shell element in the analysis of this two-sided clamped plate problem.

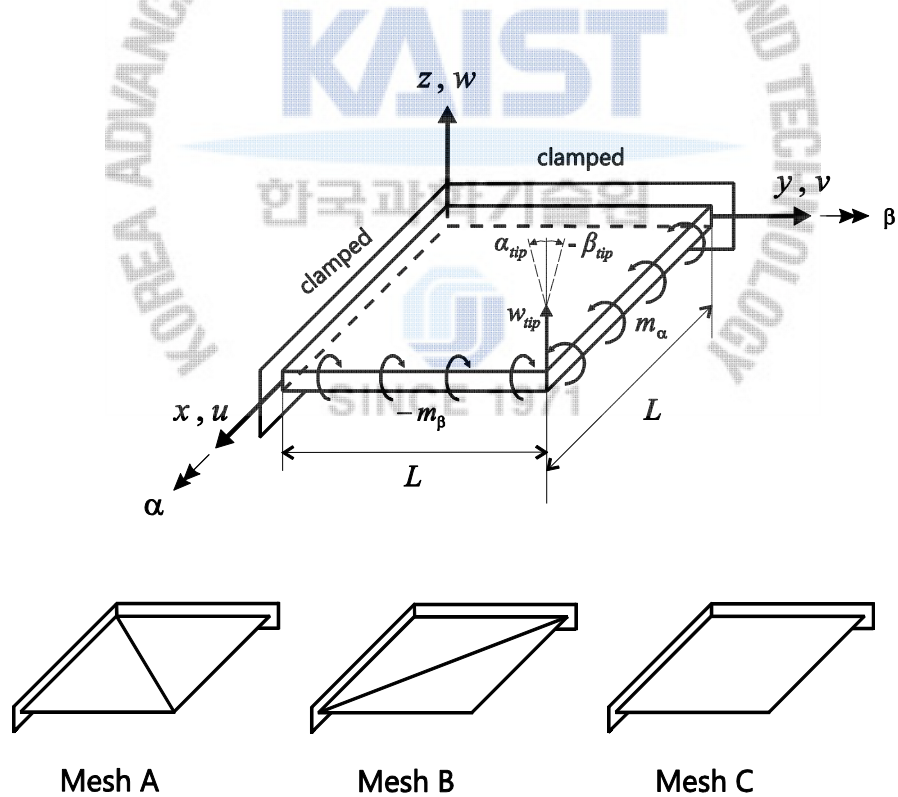


Fig. 5.7 Two-sided clamped plate problem ( $L=1.0$ ,  $m_\alpha = m_\beta = 2/L$ ,  $E=1.7472 \times 10^7$  and  $\nu=0.0$ ) and meshes used for the MITC3+shell elements (Meshes A and B) and the MITC4 shell elements (Mesh C)

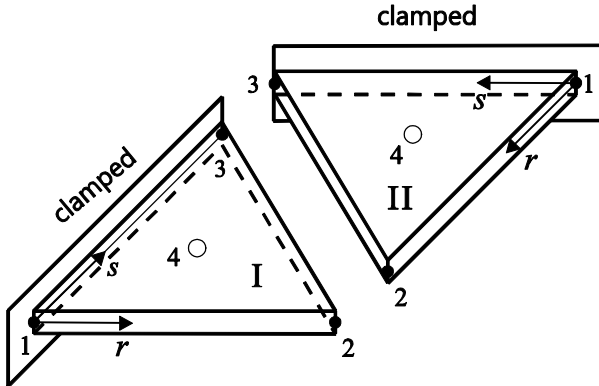


Fig. 5.8 Element node numbers for the two-sided clamped plate problem using the MITC3+ shell elements with Mesh A shown in Fig. 5.7.

### 5.3.1 Transverse shear strain fields

Using the two MITC3+ shell elements, the two-sided clamped plate is modeled by element-I and element-II as shown in Fig. 5.8. The geometry of the elements is given by the following nodal positions

$$x_1 = 1, y_1 = 0, \quad x_2 = 1, y_2 = 1, \quad x_3 = 0, y_3 = 0, \quad x_4 = 2/3, y_4 = 1/3 \quad \text{for element-I},$$

$$x_1 = 0, y_1 = 1, \quad x_2 = 1, y_2 = 1, \quad x_3 = 0, y_3 = 0, \quad x_4 = 1/3, y_4 = 2/3 \quad \text{for element-II}, \quad (5.12)$$

where the subscripts are the element node numbers, see Fig. 5.8.

The boundary condition of the elements is given by

$$u_1 = u_3 = v_1 = v_3 = w_1 = w_3 = \alpha_1 = \alpha_3 = \beta_1 = \beta_3 = 0 \quad \text{for element-I},$$

$$u_1 = u_3 = v_1 = v_3 = w_1 = w_3 = \alpha_1 = \alpha_3 = \beta_1 = \beta_3 = 0 \quad \text{for element-II}. \quad (5.13)$$

For this pure bending problem, the exact transverse shear strains are

$$e_{rt} = e_{st} = 0 \quad \text{in elements-I and II}, \quad (5.14)$$

and the theoretical relationship among the deflection  $w_2 (= w_{tip})$ , rotation  $\alpha_2 (= \alpha_{tip})$  and rotation  $\beta_2 (= \beta_{tip})$  is given, like for beams in the x- and y-directions [11], as

$$w_2 = \frac{1}{2}\alpha_2 = -\frac{1}{2}\beta_2. \quad (5.15)$$

No anticlastic curvature exists because Poisson's ratio  $\nu = 0$ . If a triangular shell element does not show shear locking, Eqs. (5.14) and (5.15) should be satisfied.

For element-I, we derive the transverse shear strain field, see Eq. (C.3) in Appendix C. Using Eqs. (5.12) and (5.13) with the symmetric condition  $\alpha_2 = -\beta_2$  in Eq. (5.15), the transverse shear strain fields for element-I and element-II are, respectively,

$$\begin{aligned} e_{rt}^I &= \frac{a}{4}(w_2 - \frac{1}{2}\alpha_2 - \frac{1}{2}\alpha_4) + \frac{1}{3}\hat{c}^I(3s-1), \\ e_{st}^I &= \frac{a}{4}(-\frac{1}{2}\beta_4) + \frac{1}{3}\hat{c}^I(1-3r) \quad \text{with} \quad \hat{c}^I = -\frac{3}{4}ad\alpha_2, \end{aligned} \quad (5.16)$$

and

$$\begin{aligned} e_{rt}^{II} &= \frac{a}{4}(w_2 + \frac{1}{2}\beta_2 + \frac{1}{2}\beta_4) + \frac{1}{3}\hat{c}^{II}(3s-1), \\ e_{st}^{II} &= \frac{a}{4}(-\frac{1}{2}\alpha_4) + \frac{1}{3}\hat{c}^{II}(1-3r) \quad \text{with} \quad \hat{c}^{II} = \frac{3}{4}ad\beta_2. \end{aligned} \quad (5.17)$$

With the tying distance  $d = 0$ , the transverse shear strains vanish with

$$w_2 - \frac{1}{2}\alpha_2 - \frac{1}{2}\alpha_4 = 0, \quad \beta_4 = 0 \quad \text{for element-I}, \quad (5.18)$$

$$w_2 + \frac{1}{2}\beta_2 + \frac{1}{2}\beta_4 = 0, \quad \alpha_4 = 0 \quad \text{for element-II}. \quad (5.19)$$

When  $\alpha_4 = 0$  in Eq. (5.18) and  $\beta_4 = 0$  in Eq. (5.19), the pure bending condition is satisfied with

$$w_2 - \frac{1}{2}\alpha_2 = 0, \quad w_2 + \frac{1}{2}\beta_2 = 0. \quad (5.20)$$

This result shows that the MITC3+ shell element can correctly represent the pure bending conditions in Eqs. (5.14) and (5.15) when  $d = 0$ . Similarly, we tested the MITC3+ shell element in Mesh B and observed that the elements in Mesh B also satisfy the pure bending conditions. Of course, the MITC3 shell element does not satisfy the pure bending conditions in Mesh A and thus shear locking occurs [11].

Table 5.7 Strain energies for the two-sided clamped plate problem shown in Fig. 5.7. The tying distance  $d = 0$  is used for the MITC3+ shell element.

$a/L$	Mesh A		Mesh B		Mesh C
	MITC3	MITC3+	MITC3	MITC3+	MITC4
1/100	4.1190E-04	4.8858E-01	6.8681E-01	6.8681E-01	1.0989E+00
1/1,000	4.1209E-03	4.8840E+02	6.8681E+02	6.8681E+02	1.0989E+03
1/10,000	4.1209E-02	4.8840E+05	6.8681E+05	6.8681E+05	1.0989E+06
Order of change	$a/L$	$(a/L)^3$	$(a/L)^3$	$(a/L)^3$	$(a/L)^3$

### 5.3.2 Strain energy

Considering three different thicknesses(1/100, 1/1,000 and 1/10,000), we next solve the two-sided clamped plate problem using the MITC3, MITC3+ and MITC4 shell elements with the applied moments  $m_\alpha = m_\beta = 2/L$ , see Fig. 5.7.

Table 5.7 presents the strain energies calculated using the MITC3, MITC3+ ( $d = 0$ ) and MITC4 shell elements, respectively. Analytically, the calculated strain energy should change in the order of  $(a/L)^3$  for this pure bending problem [2]. The MITC3 shell element shows correct results only in Mesh B. The MITC3+ shell element shows correct behaviors in both Meshes A and B, although the solutions depend on the mesh patterns. The MITC4 shell element obviously shows excellent results.

Changing the tying distance  $d$  in the assumed transverse shear strain field of the MITC3+ shell element, we investigate the strain energy stored in the two-sided clamped plate problem with Mesh A. Four different tying distances are considered: 1/100, 1/1,000, 1/10,000 and 1/100,000. Table 5.8 shows that, as the distance  $d$  approaches zero, the behavior of the MITC3+ shell element become better.

Note that the bending mode BL1 of the assemblage of two right-angled triangular elements is significantly present in the pure bending displacement field of the problem with Mesh A. Thus, the improved behavior of the MITC3+ shell element is directly due to the alleviation of shear locking in this mode.

Table 5.8 Strain energies for the two-sided clamped plate problem shown in Fig. 5.7 using the Mesh A with the MITC3+ shell elements according to the tying distance  $d$ .

$a/L$	$d$	1/100	1/1,000	1/10,000	1/100,000
1/100		1.5589E-01	4.7837E-01	4.8848E-01	4.8858E-01
1/1,000		2.2787E+00	1.5587E+02	4.7820E+02	4.8830E+02
1/10,000		2.2893E+01	2.2787E+03	1.5587E+05	4.7820E+05

#### 5.4 Dynamic mode analysis

In this section, the dynamic mode analysis is performed to investigate the predictive capability of the MITC3 and MITC3+ shell elements in dynamic analysis. Frequencies and modes are calculated and the results are compared with those of the MITC4 shell element. Hence, two benchmark problems are considered: a free square plate problem and a free hyperboloid shell problem [10, 24, 56-64].

For dynamic mode analysis, the following eigenvalue problem is solved

$$\mathbf{K}\vec{\phi}_i^d = \lambda_i^d \mathbf{M}\vec{\phi}_i^d \quad \text{with} \quad \lambda_i^d = \omega_i^2 \quad \text{and} \quad i=1,2,\dots,N, \quad (5.21)$$

where  $\mathbf{K}$  and  $\mathbf{M}$  is the stiffness and consistent mass matrices, respectively,  $\lambda_i^d$  is the eigenvalue(the square of the free vibration frequency  $\omega_i$ ,  $\lambda_i^d = \omega_i^2$ ),  $\vec{\phi}_i^d$  is the corresponding M-orthonormal eigenvector (dynamic mode), and  $N$  is the number of the degrees of freedom [1]. Note that, unlike in static mode analysis, both stiffness and mass matrices are considered in dynamic mode analysis.

To measure the convergence of the finite element solutions in dynamic mode analysis, we use the relative error in the reciprocal frequencies as follows

$$e_h = \left| \frac{1/\omega_{ref} - 1/\omega_h}{1/\omega_{ref}} \right| = \left| 1 - \frac{\omega_{ref}}{\omega_h} \right|, \quad (5.22)$$

in which  $\omega_{ref}$  is the reference frequency,  $\omega_h$  is the frequency of the finite element discretization. The analytical solution is not available for  $\omega_{ref}$  in the considered benchmark problems. Hence, the reference frequency  $\omega_{ref}$  is obtained using very fine meshes of the MITC4 shell element.

For the dynamic analysis of the shell problems, the optimal convergence behavior of the elements is given by

$$e_h \cong Ch^k, \quad (5.23)$$

where  $h$  is the element size. For a 3-node shell element to be uniformly optimal, the value of  $C$  must be constant, that is, independent of the shell thickness, and  $k=2$  [62, 63].

#### 5.4.1 Free square plate problem

A free square plate of dimensions  $L \times L$  shown is considered, see Fig. 5.9.  $L=1.0$ ,  $E=2.07 \times 10^{11}$ ,  $\nu=0.3$  and density  $\rho=7.8 \times 10^3$  are used. No boundary condition is imposed. The reference solutions are obtained using a  $50 \times 50$  element mesh of the MITC4 shell elements and verified by Refs. [60, 61].

Table 5.9 presents the frequencies calculated with  $N \times N$  element meshes ( $N=5, 10, 15$  and  $20$ ) when  $a/L=1/1,000$ . The frequencies of the modes 7 to 9 are close to the reference solutions for all tested elements. The frequencies corresponding to modes 10 and 11 should be identical, but this can hardly be the case using triangular shell elements due to the non-symmetry in the mesh patterns used. While the MITC3 shell element produces considerably different frequencies for modes 10 and 11, the MITC3+ shell element shows very similar frequencies for the modes. Using the MITC4 and MITC3+ shell elements produces much more accurate frequencies than obtained with the MITC3 shell element. In Fig. 5.10, we see that the MITC3 shell element produces a wrong mode shape for the 11th frequency.

The convergence curves of the 10th and 11th frequencies are plotted in Fig. 5.11. Three different thicknesses ( $a/L=1/100, 1/1,000$  and  $1/10,000$ ) are considered. The shell finite element solutions are calculated using four different  $N \times N$  element meshes ( $N=5, 10, 15$  and  $20$ ). We observe that the performance of the MITC3 shell element deteriorates as the thickness decreases, that is, locking occurs. However, the MITC3+ and MITC4 shell elements show, similarly, excellent convergence.

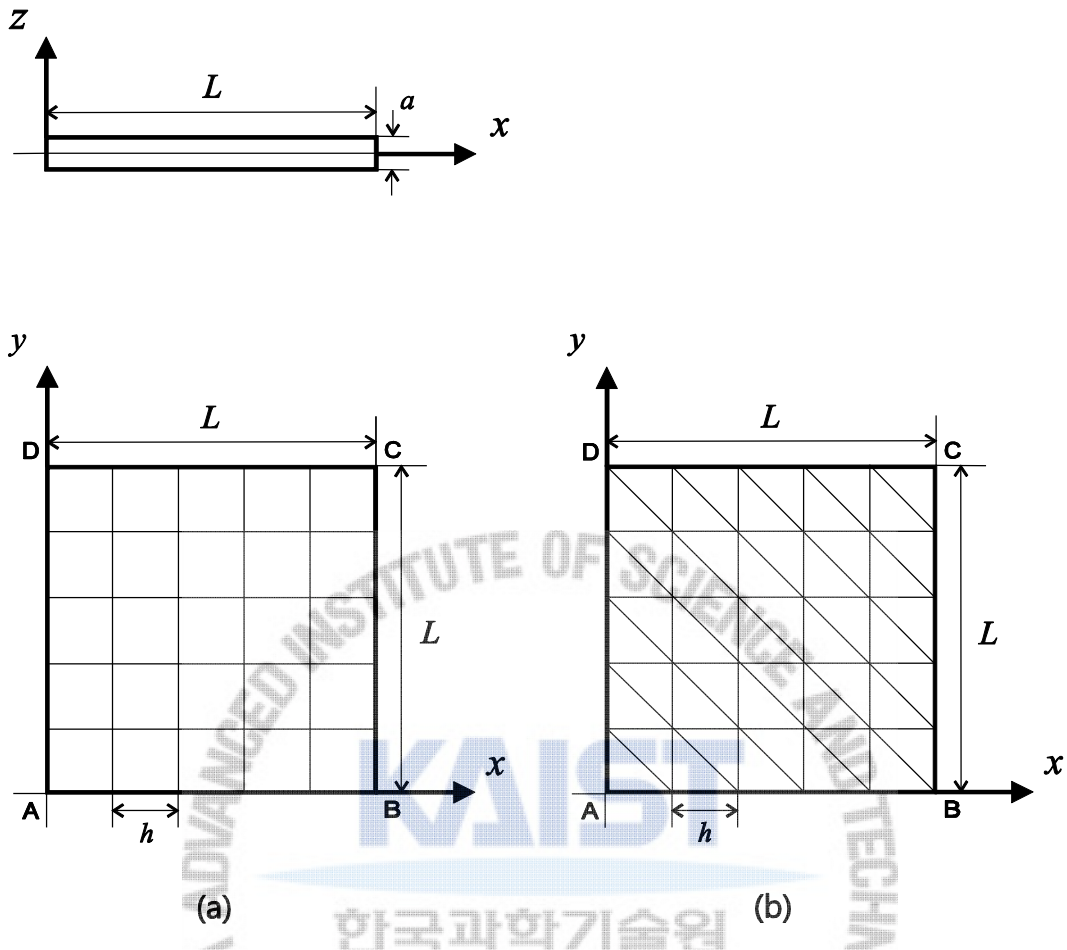


Fig. 5.9 Free square plate problem for dynamic mode analyses with 2 different  $5 \times 5$  mesh patterns ( $L=1.0$ ,  $E=2.07 \times 10^{11}$ ,  $\nu=0.3$  and  $\rho=7.8 \times 10^3$ ). (a) Mesh pattern used for quadrilateral shell elements. (b) Mesh pattern used for triangular shell elements.

The distorted mesh shown in Fig 5.12 is considered. When an  $N \times N$  element mesh is used, each edge is discretized in the following ratio:  $L_1 : L_2 : L_3 : \dots : L_N = 1 : 2 : 3 : \dots : N$ . Table 5.10 presents the frequencies with distorted  $N \times N$  element meshes ( $N=5, 10, 15$  and  $20$ ) when  $a/L=1/1,000$ . Fig. 5.13 shows the convergence curves of the 10th and 11th frequencies. In both results, the MITC3+ and MITC4 shell elements still show good results even though the modes 10 and 11 are slightly different.

Table 5.9 Frequencies of the modes 7-11 for the free plate problem shown in Fig. 5.9 with  $N \times N$  meshes when  $a/L = 1/1,000$ .

Shell elements	$N$	Mode number				
		7	8	9	10	11
MITC4	5	21.366	31.922	40.568	57.223	57.223
	10	21.094	30.915	38.547	55.067	55.067
	15	21.040	30.714	38.153	54.619	54.619
	20	21.021	30.642	38.015	54.459	54.459
MITC3	5	21.738	31.964	40.687	60.007	118.46
	10	21.647	30.986	38.684	57.523	101.67
	15	21.576	30.787	38.284	56.845	98.340
	20	21.468	30.710	38.129	56.273	84.032
MITC3+	5	21.247	31.677	40.017	57.568	57.908
	10	21.051	30.862	38.431	55.088	55.451
	15	21.011	30.690	38.103	54.601	54.783
	20	20.998	30.629	37.986	54.434	54.540
Ref.		21.000	30.564	37.864	54.284	54.284

\* The reference solutions are obtained by a  $50 \times 50$  element meshes of MITC4 shell elements.

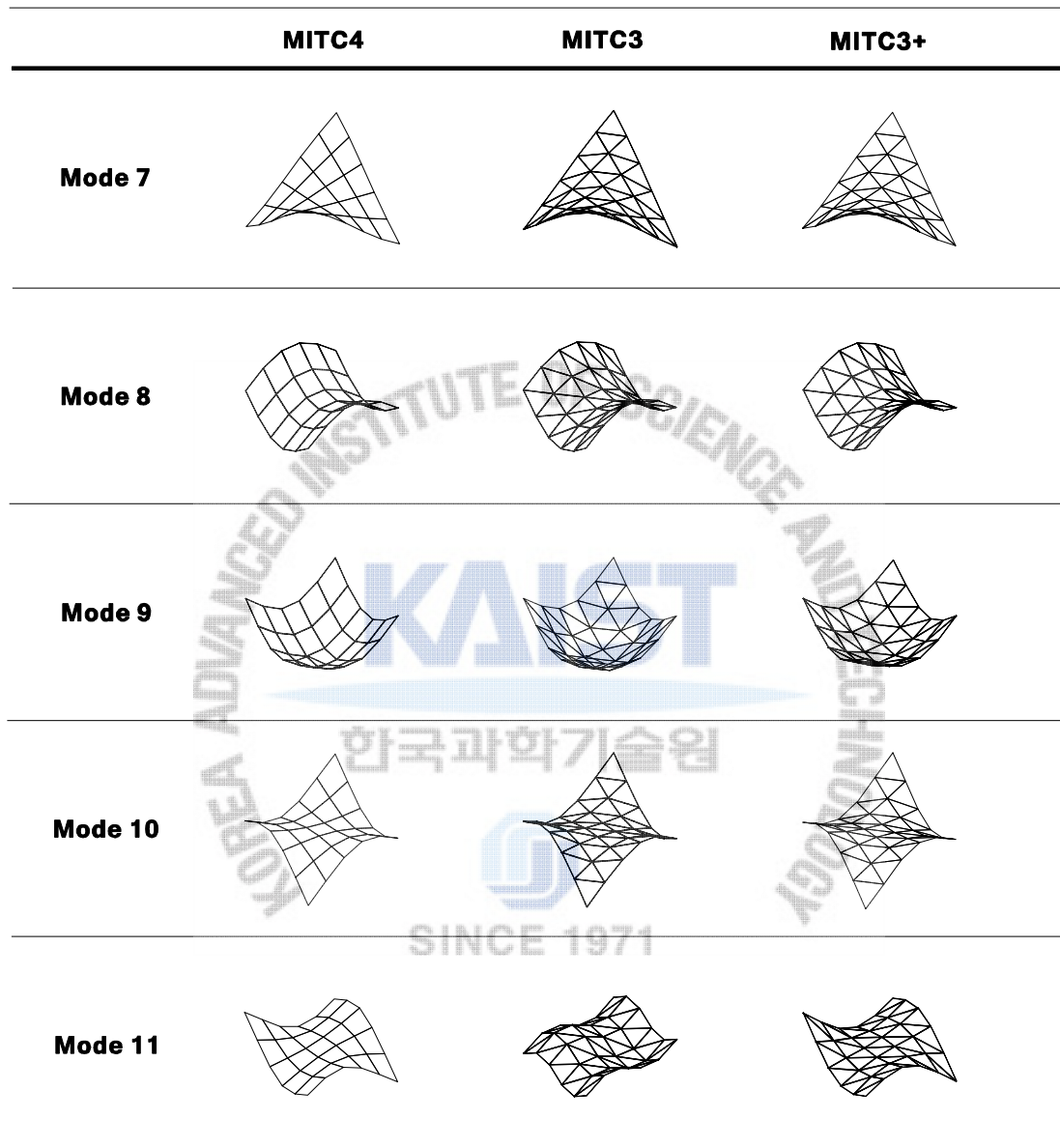
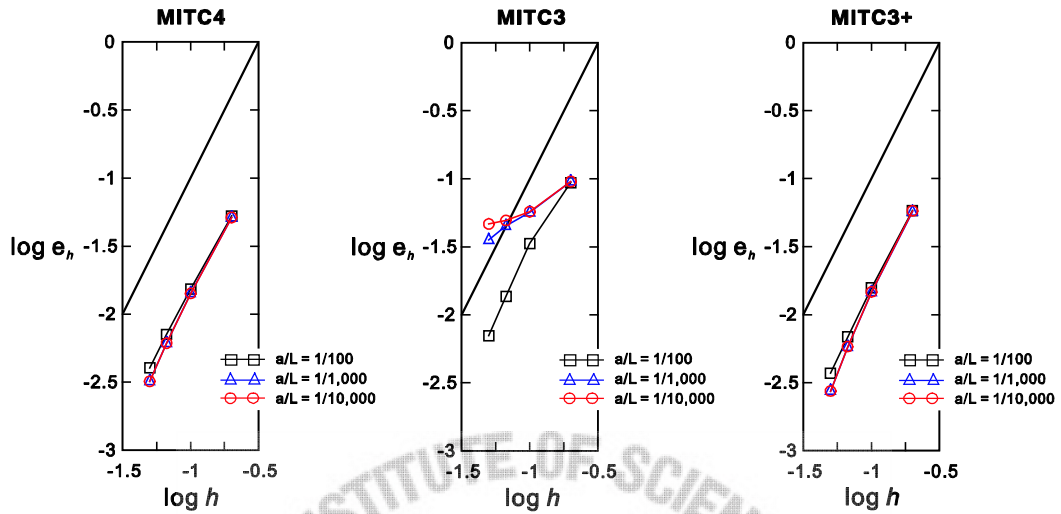
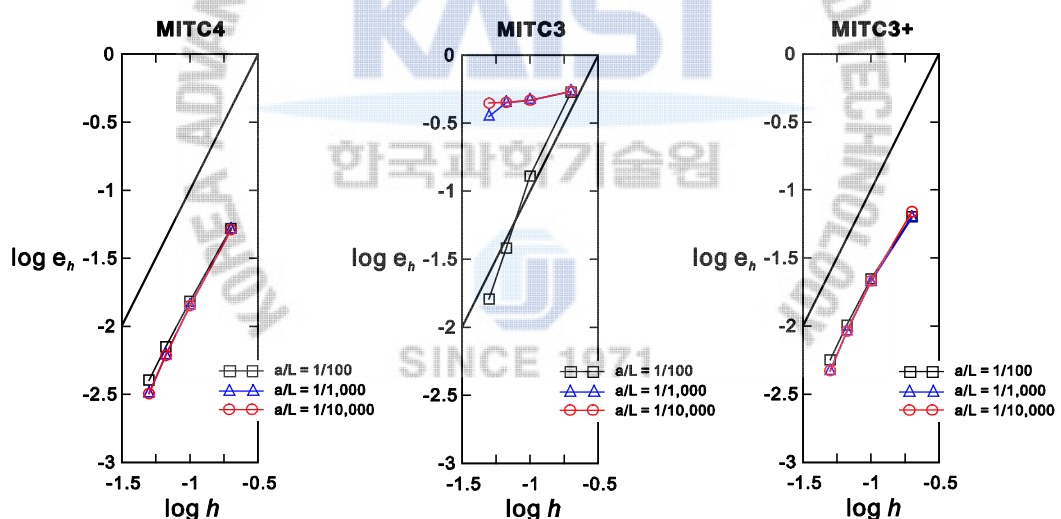


Fig. 5.10 Shapes of the modes 7-11 for the free plate problem shown in Fig. 5.9 with  $5 \times 5$  element meshes when  $a/L = 0.001$ .



(a) Mode 10



(b) Mode 11

Fig. 5.11 Convergence curves of the 10th and 11th frequencies for the free plate problem. The solutions of the shell elements are obtained with uniform  $N \times N$  element meshes ( $N = 5, 10, 15$  and  $20$ ). The bold line represents the optimal convergence rate.

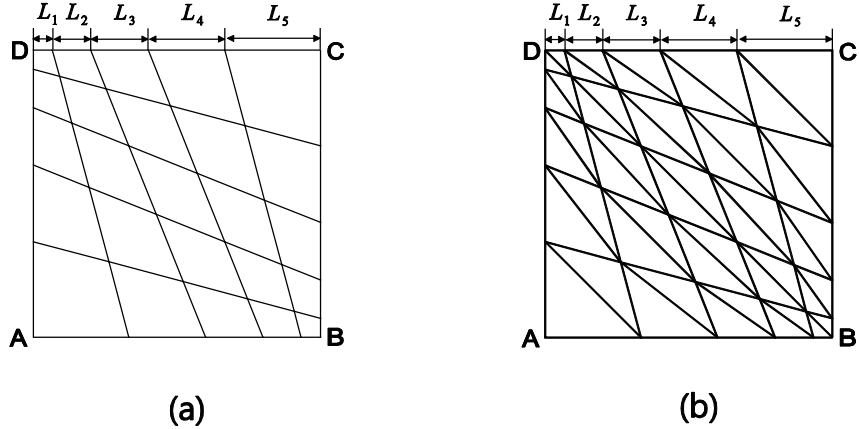


Fig. 5.12 Distorted mesh pattern for  $N=5$ . (a) Quadrilateral shell elements. (b) Triangular shell elements.

#### 5.4.2 Free hyperboloid shell problem

The free hyperboloid shell shown in Fig. 5.14 is considered. The mid-surface of the shell structure is given by [10,24]

$$x^2 + z^2 = 1 + y^2; \quad y \in [-1, 1]. \quad (5.24)$$

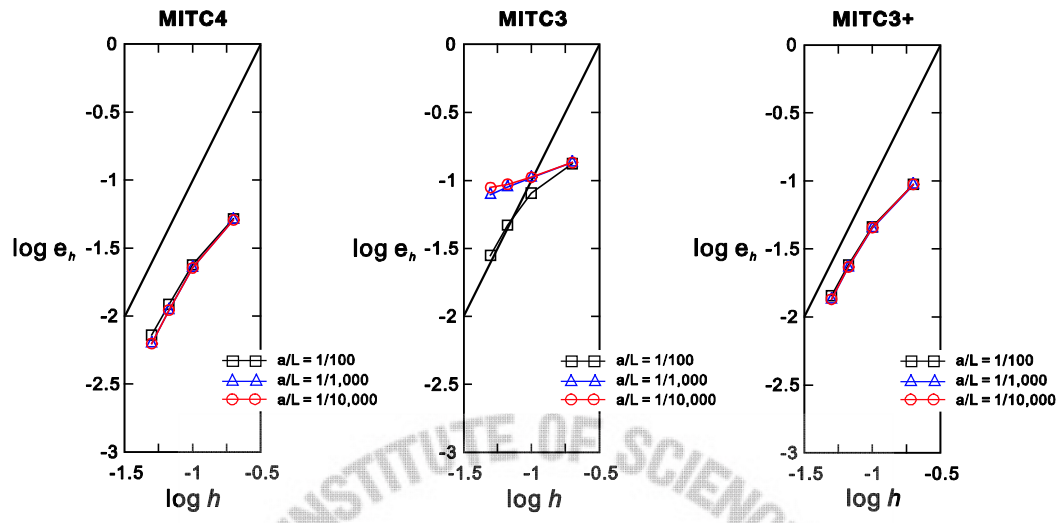
We use  $L=1.0$ ,  $E=2.0 \times 10^{11}$ ,  $\nu=1/3$  and  $\rho=7.8 \times 10^3$ . No boundary condition is imposed.

Table 5.11 presents the frequencies calculated with uniform  $4N$  (circumferential direction)  $\times 2N$  (longitudinal direction) element meshes ( $N=5, 10, 15$  and  $20$ ) when  $a/L=1/1,000$ . The reference solutions are obtained using a  $200 \times 100$  uniform mesh of the MITC4 shell elements. For all the elements tested, the frequencies 7, 9 and 11 are identical to the frequencies 8, 10 and 12, respectively. Using the MITC4 and MITC3+ shell elements produces much more accurate frequencies than obtained with the MITC3 shell element. Fig. 5.15 displays the shapes of the modes 7-12 for uniform  $20 \times 10$  element meshes. The mode shapes of the MITC3+ shell element are similar to those of the MITC4 shell element.

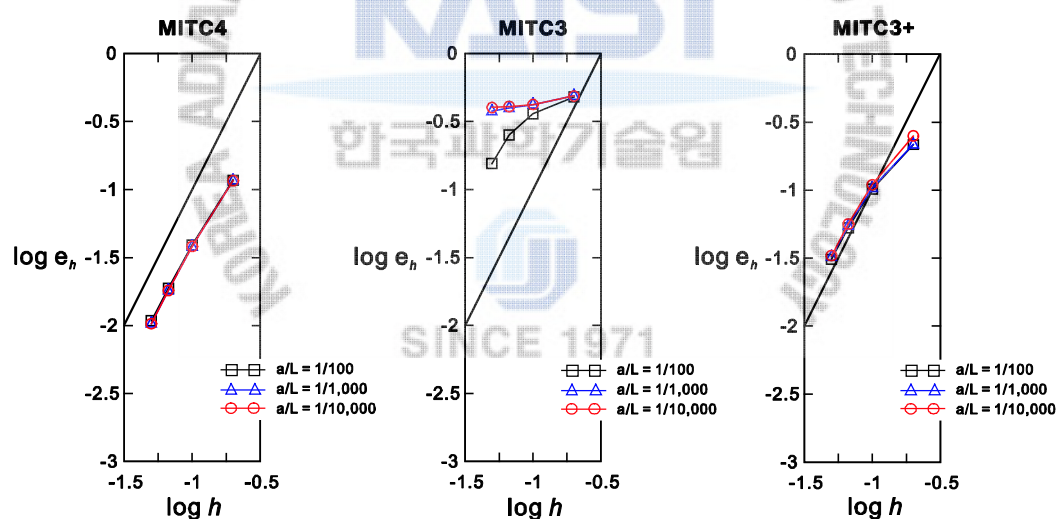
Table 5.10 Frequencies of the modes 7-11 for the free square plate problem with  $N \times N$  distorted meshes shown in Fig. 5.12 when  $a/L = 1/1,000$ .

Shell elements	$N$	Mode number				
		7	8	9	10	11
MITC4	5	21.575	33.071	42.004	57.191	61.420
	10	21.189	31.311	39.109	55.541	56.437
	15	21.087	30.908	38.436	54.892	55.286
	20	21.049	30.757	38.183	54.628	54.851
MITC3	5	22.184	33.780	43.522	62.781	105.68
	10	21.812	32.397	40.587	60.633	93.456
	15	21.692	32.053	39.838	59.615	89.827
	20	21.630	31.829	39.445	58.909	87.021
MITC3+	5	21.817	33.177	43.060	59.889	69.344
	10	21.318	31.546	39.651	56.842	60.559
	15	21.148	31.052	38.734	55.571	57.419
	20	21.079	30.848	38.366	55.026	56.096
Ref.		21.000	30.564	37.864	54.284	54.284

\* The reference solutions are obtained by a  $50 \times 50$  element meshes of the MITC4 shell elements.



(a) Mode 10



(b) Mode 11

Fig. 5.13 Convergence curves of the 10th and 11th frequencies for the free plate problem with the distorted meshes shown in Fig. 5.12. The bold line represents the optimal convergence rate.

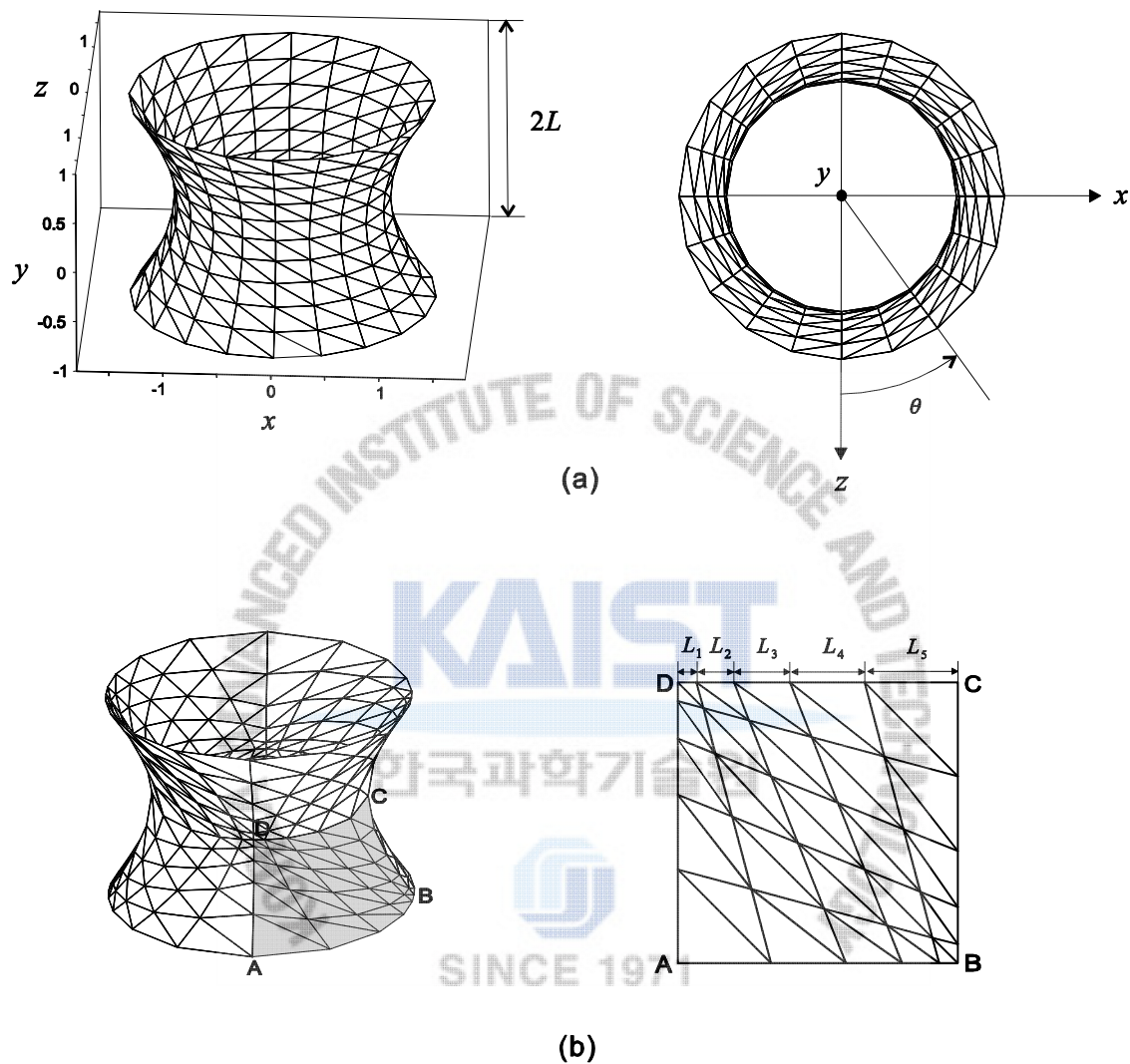


Fig. 5.14 Free hyperboloid shell problem ( $L=1.0$ ,  $E=2.0\times 10^{11}$ ,  $\nu=1/3$  and  $\rho=7.8\times 10^3$ ). (a) Problem description with the uniform mesh. (b) Distorted mesh pattern.

Table 5.11 Frequencies of the modes 7-12 for the free hyperboloid shell problem with the  $4N \times 2N$  uniform meshes shown in Fig. 5.14(a) when  $a/L = 1/1,000$ .

Shell elements	$N$	Mode number					
		7	8	9	10	11	12
MITC4	5	4.0562	4.0562	6.8339	6.8339	13.163	13.163
	10	4.0089	4.0089	6.7965	6.7965	12.808	12.808
	15	3.9976	3.9976	6.7903	6.7903	12.745	12.745
	20	3.9924	3.9924	6.7882	6.7882	12.721	12.721
MITC3	5	37.449	37.449	149.20	149.20	157.83	157.83
	10	10.029	10.029	35.321	35.321	39.830	39.830
	15	6.0202	6.0202	16.534	16.534	21.429	21.429
	20	4.9650	4.9650	10.734	10.734	16.452	16.452
MITC3+	5	4.1610	4.1610	7.0337	7.0337	13.781	13.781
	10	4.0309	4.0309	6.8420	6.8420	12.969	12.969
	15	4.0091	4.0091	6.8096	6.8096	12.819	12.819
	20	4.0010	4.0010	6.7986	6.7986	12.767	12.767
Ref.		3.9830	3.9830	6.7859	6.7859	12.690	12.690

\* The reference solutions are obtained by  $200 \times 100$  element meshes of MITC4 shell element.

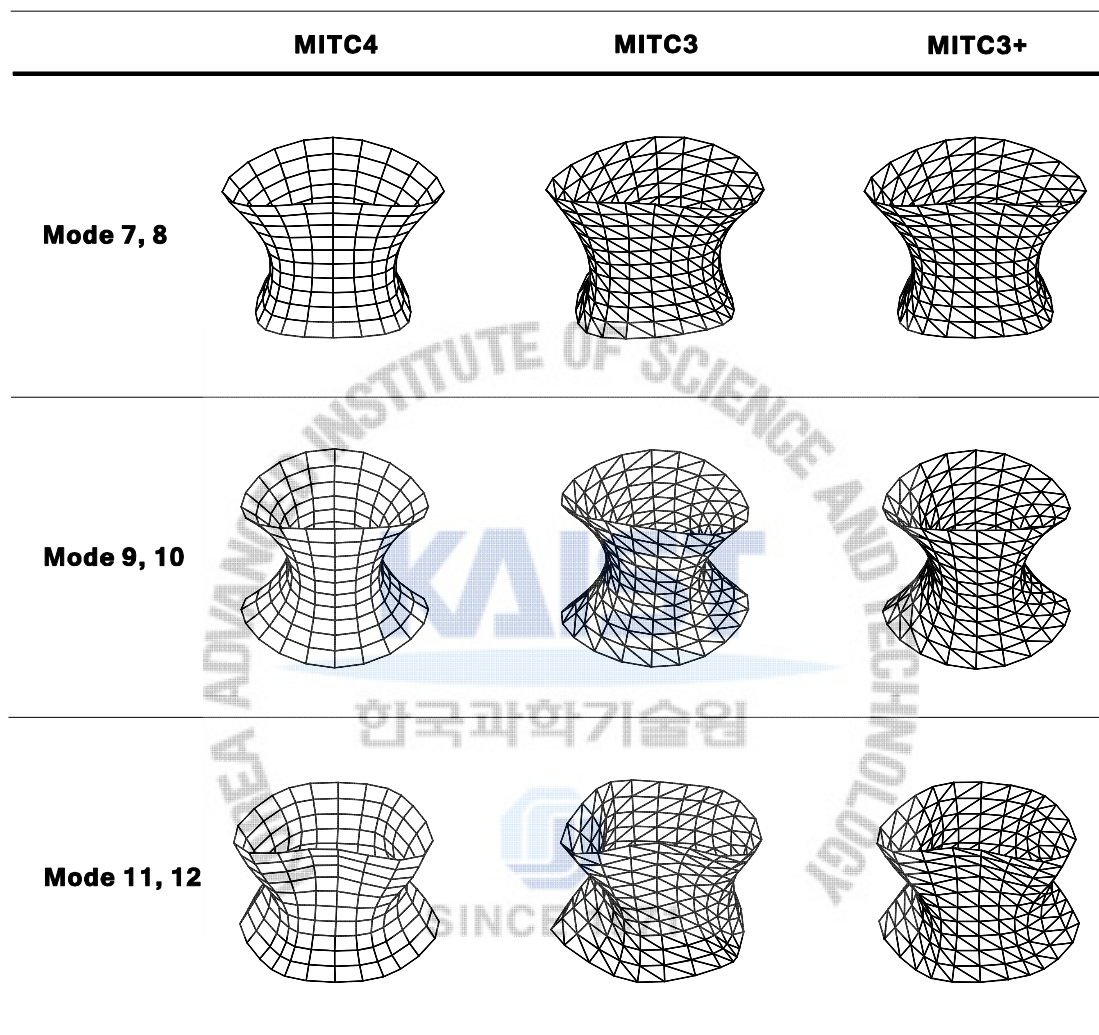


Fig. 5.15 Shapes of the modes 7-12 for the free hyperboloid shell problem shown in Fig. 14(a) with  $20 \times 10$  element meshes when  $a/L = 0.001$ .

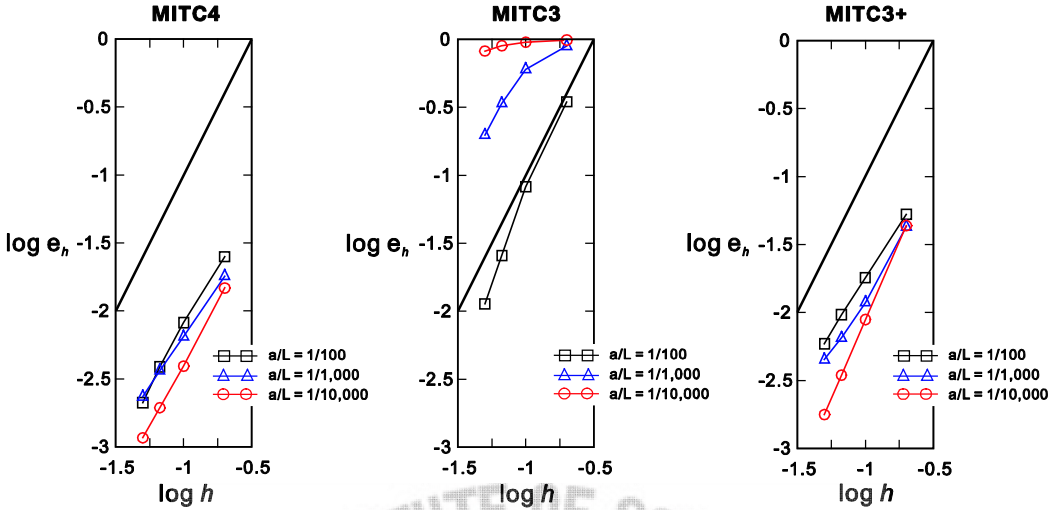


Fig. 5.16 Convergence curves of the 7th and 8th frequencies for the free hyperboloid shell problem with the uniform meshes shown in Fig. 5.14(a). The solutions of the shell elements are obtained with uniform  $4N \times 2N$  element meshes ( $N = 5, 10, 15$  and  $20$ ). The bold line represents the optimal convergence rate.

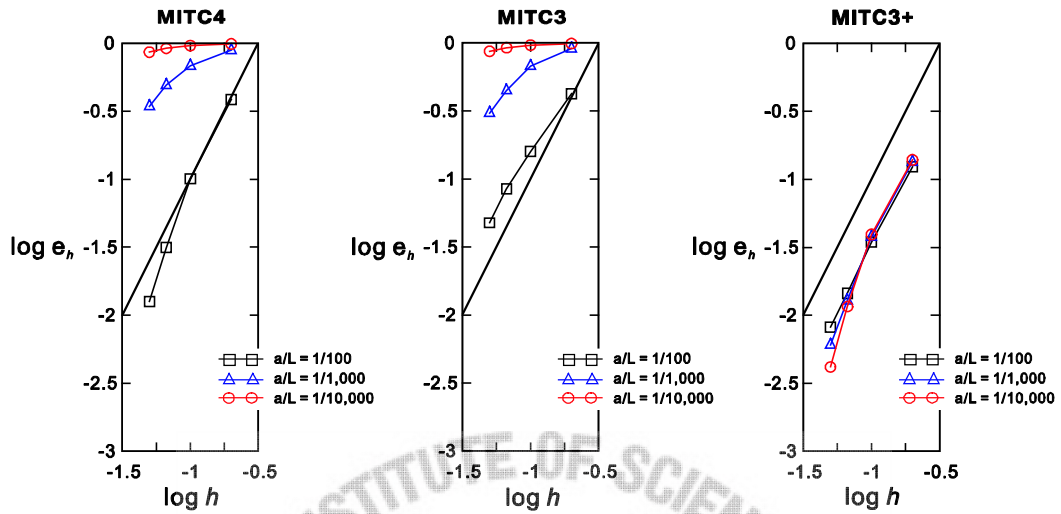
Fig. 5.16 displays the convergence curves of the 7th and 8th frequencies for three different thicknesses:  $a/L = 1/100$ ,  $1/1,000$ , and  $1/10,000$ . The MITC3+ shell element displays good convergence behaviors similar to the MITC4 shell element. As the thickness decreases, the convergence of the MITC3 shell element becomes worse due to locking.

Also, the distorted mesh shown in Fig 5.14(b) is considered. Using the shaded region in Fig. 14(b), each edge is discretized by the following ratio:  $L_1 : L_2 : L_3 : \dots : L_N = 1 : 2 : 3 : \dots : N$ . Table 5.12 presents the frequencies with distorted  $4N \times 2N$  element meshes ( $N = 5, 10, 15$  and  $20$ ) when  $a/L = 1/1,000$ . Fig. 5.17 shows the convergence curves of the 7th and 8th frequencies. In both results, we observe that, while the MITC4 and MITC3 shell elements lock, the MITC3+ shell element still shows good results.

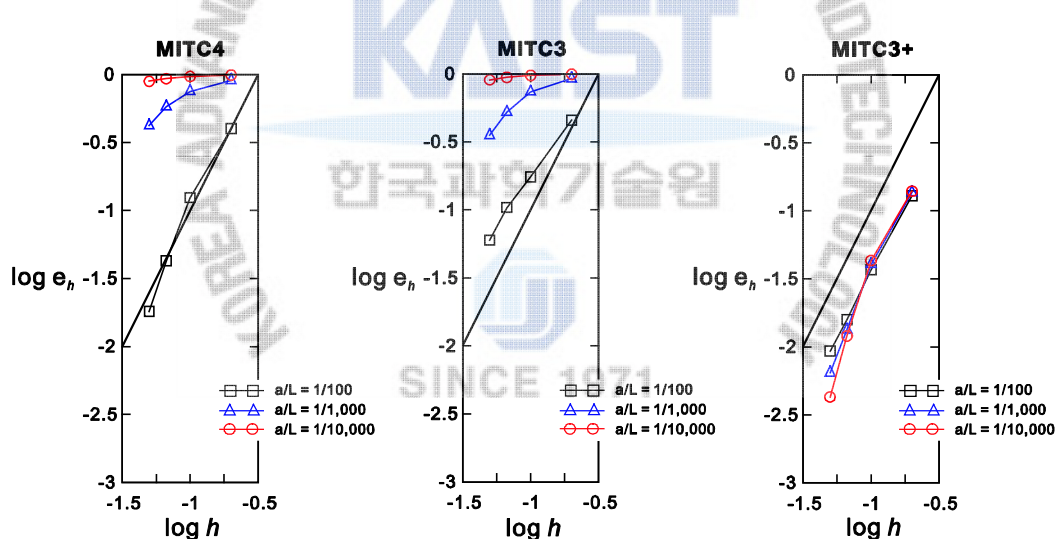
Table 5.12 Frequencies of the modes 7-12 for the free hyperboloid shell problem with the  $4N \times 2N$  distorted meshes shown in Fig. 5.14(b) when  $a/L = 1/1,000$ .

Shell elements	$N$	Mode number					
		7	8	9	10	11	12
MITC4	5	35.751	43.056	44.075	78.905	102.856	123.838
	10	12.537	16.050	17.223	28.059	42.093	43.224
	15	7.8465	9.4797	11.936	16.397	25.840	26.525
	20	6.0587	6.8917	9.7234	11.844	19.647	19.995
MITC3	5	43.052	51.536	168.76	203.23	221.47	228.83
	10	12.338	15.239	44.835	56.487	59.559	80.330
	15	7.2037	8.3684	22.653	29.413	30.099	40.473
	20	5.7356	6.1662	15.218	20.757	21.105	24.968
MITC3+	5	4.6031	4.6142	8.5172	8.5405	15.019	15.034
	10	4.1392	4.1514	7.0032	7.1431	13.316	13.343
	15	4.0347	4.0368	6.8320	6.8816	12.867	12.881
	20	4.0073	4.0090	6.7988	6.8250	12.738	12.748
Ref.		3.9830	3.9830	6.7859	6.7859	12.690	12.690

\* The reference solutions are obtained by  $200 \times 100$  element meshes of MITC4 shell element.



(a) Mode 7



(b) Mode 8

Fig. 5.17 Convergence curves of the 7th and 8th frequencies for the free hyperboloid shell problem with the distorted meshes shown in Fig. 5.14(b). The bold line represents the optimal convergence rate.

## 5.5 Closure

In this chapter, the static and dynamic modal behaviors of the MITC3+ triangular shell element are studied. For comparison, also the DISP3, MITC3 and MITC4 shell elements were considered.

The detailed static mode analyses were performed for the single right-angled triangular shell element and the assemblage of two right-angled triangular shell elements. We also investigated the transverse shear strain fields of the MITC3+ shell element in the two-sided clamped plate problem. Through these studies, we found that, in the MITC3+ shell element, additional antisymmetric bending modes ( $B1^+$  and  $B2^+$ ) are activated due to bubble function enrichment and shear locking is alleviated in those modes by using the MITC method. Consequently, unlike the DISP3 and MITC3 shell elements, the MITC3+ shell element does not lock in two element assemblages as well as in a single element.

Dynamic mode analyses are performed considering the free square problem and the free hyperboloid shell problem. The frequencies and mode shapes are investigated. The MITC3+ shell element shows much better behaviors than the MITC3 shell element. Indeed, the MITC3+ shell element gives as accurate results as the MITC4 shell element in the uniform meshes. Even when the distorted mesh is used, the MITC3+ shell element still presents good results.



## Chapter 6.Performance of 3-node shell elements for classical benchmark problems

In this chapter, several classical benchmark problems are considered to assess the performance using the following MITC shell elements and other 3-node triangularshell elements [65-70].

- MITC3: 3-nodetriangular shell element based on the MITC method [10]
- MITC3+: 3-node triangular shell element enriched by a cubic bubble function on rotations using the MITC method[24]
- MITC3i: MITC3+ triangular shell element without a cubic bubble function [24]
- MITC4: 4-node quadrilateral shell element based on the MITC method [19]
- A3: 3-node triangular shell elementin ANSYS [66]
- S3: 3-node triangular shell element in ABAQUS[67]

In benchmark shell problems, to measure the performance in the finite element solution, the displacement normalized by the reference solution is used.

### 6.1 Fully clamped square plate problem



The plate bending problem shown in Fig. 6.1 is considered. A square plate of dimensions  $2L \times 2L$  with uniform thickness  $t$  is subjected to both loading cases. One loading case is the concentrated load  $P$  at the center of the plate. The other loading case is the uniform pressure  $q$  normal to the flat surface. All the edges are fully clamped. Due to symmetry, only a one-quarter model is considered.

For the reference solution, based on Kirchhoff theory, the central displacement due to concentrated load  $P$  is given by [68]

$$w_C^{ref}(P) = 0.0056 \frac{P(2L)^2}{D}. \quad (6.1)$$

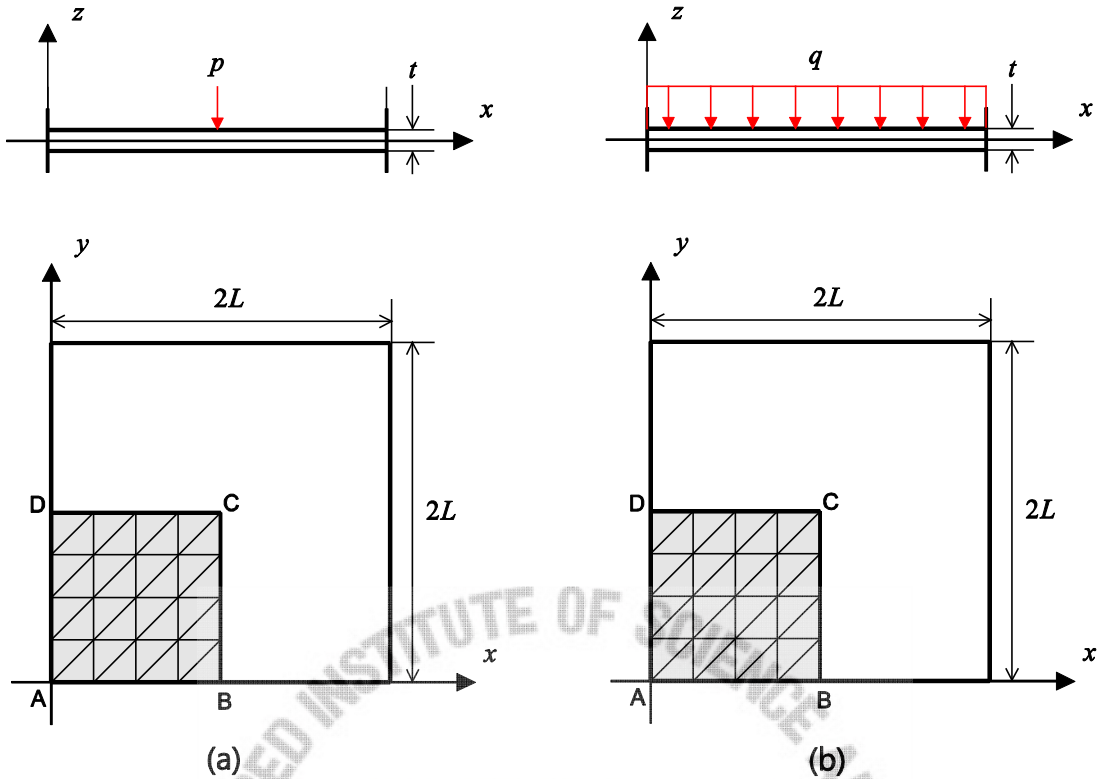


Fig. 6.1 Fully clamped square plate problem ( $L=1.0$ ,  $E=1.7472 \times 10^7$  and  $\nu=0.3$ ). (a) Concentrated load ( $p=4.0$ ). (b) Uniform pressure ( $q=1.0$ ).

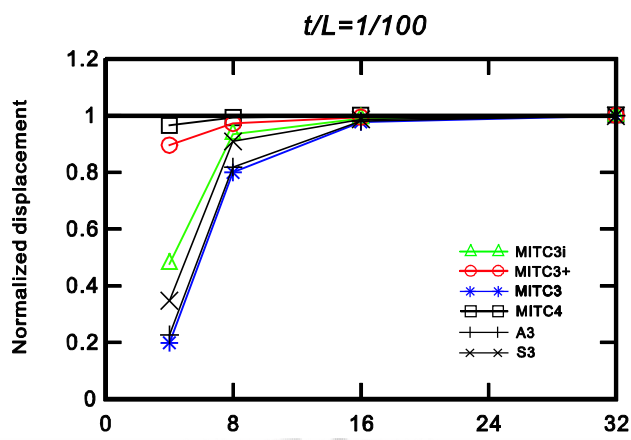
The central displacement due to the uniform pressure  $q$  normal to the flat surface is obtained by

$$w_C^{ref}(q) = 0.00126 \frac{q(2L)^2}{D}, \quad (6.2)$$

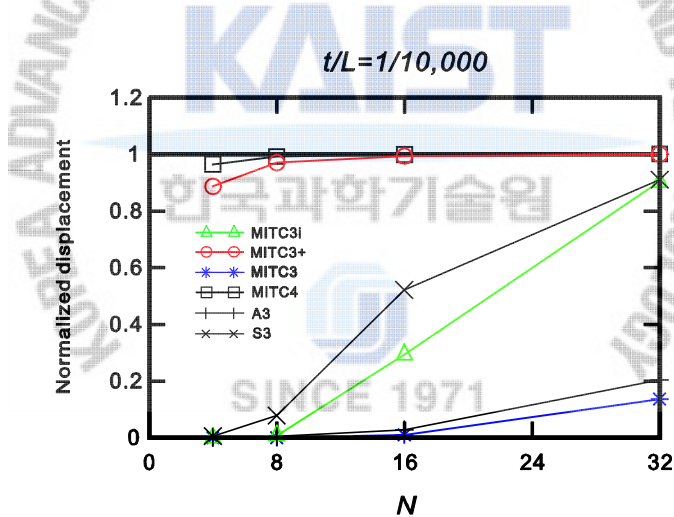
where  $D$  is the flexural rigidity of the plate given by

$$D = \frac{Et^3}{12(1-\nu^2)}. \quad (6.3)$$

Fig. 6.2 and 6.3 present the convergence curves for the normalized displacements ( $w_C$ ) at the center in both concentrated load and uniform pressure cases, respectively. We use  $N \times N$  element meshes ( $N = 4, 8, 16$ , and 32) to calculate the solutions using the shell elements. The performance of the MITC3+ shell element is much better than that of the other triangular shell elements. Also, the convergence behavior of the MITC3+ shell element is as good as that of the quadrilateral MITC4 shell element.

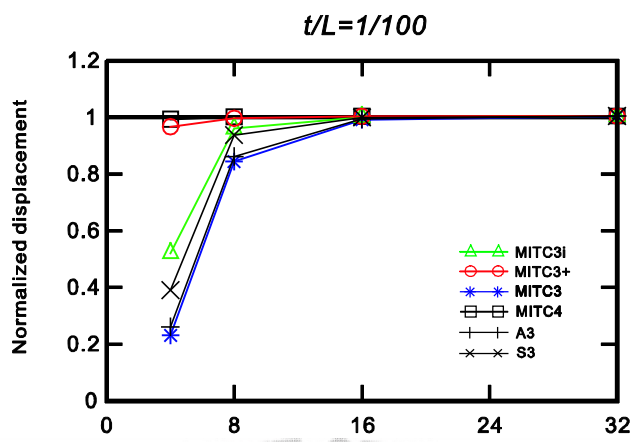


(a)

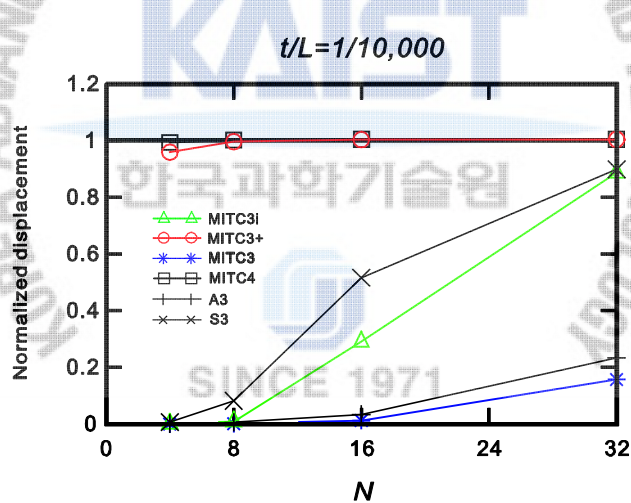


(b)

Fig. 6.2 Convergence curves of the normalized displacements ( $w_C$ ) for the fully clamped square plate problem under the concentrated load.



(a)



(b)

Fig. 6.3 Convergence curves of the normalized displacements ( $w_C$ ) for the fully clamped square plate problem under the uniform pressure.

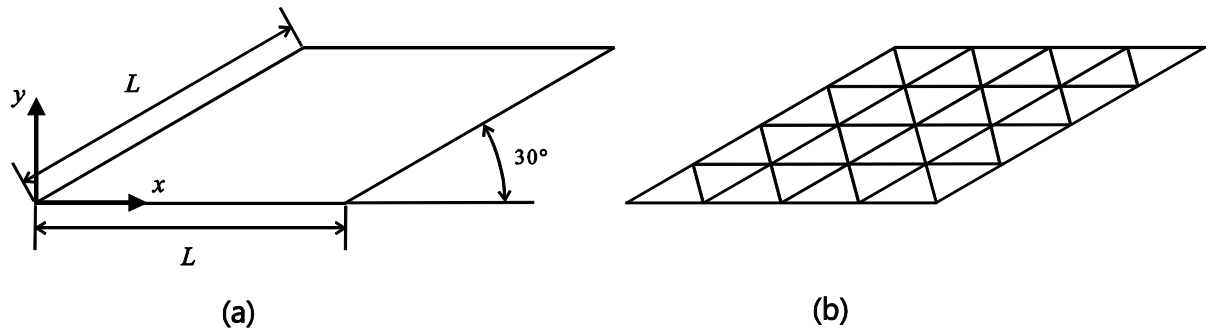


Fig. 6.4 Morley's thirty-degree skew plate problem ( $L = 100$ ,  $E = 1.0 \times 10^7$  and  $\nu = 0.3$ ). (a) Problem description. (b) Mesh pattern used for  $N = 4$ .

### 6.2 Morley's thirty-degree skew plate problem.

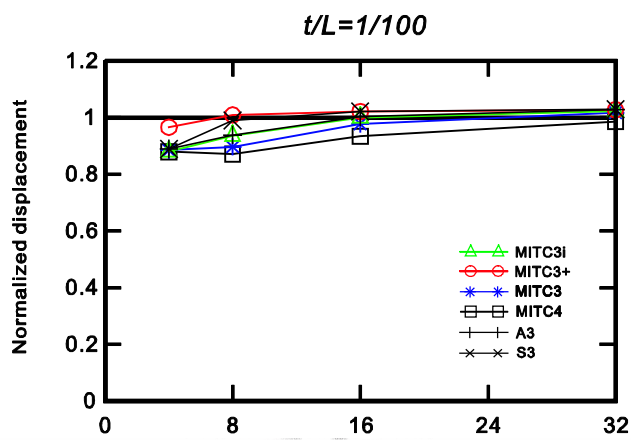
The simply supported thirty-degree skew plate with edges of  $L$  and uniform thickness  $t$  is subjected to uniform pressure ( $q = 1$ ) normal to the flat surface, as shown in Fig. 6.4. The boundary condition  $u_z = 0$  is imposed along all edges. For the reference solution, the central displacement is given by [69]

$$w_{center}^{ref}(q) = 0.000408 \frac{qL^4}{D}. \quad (6.4)$$

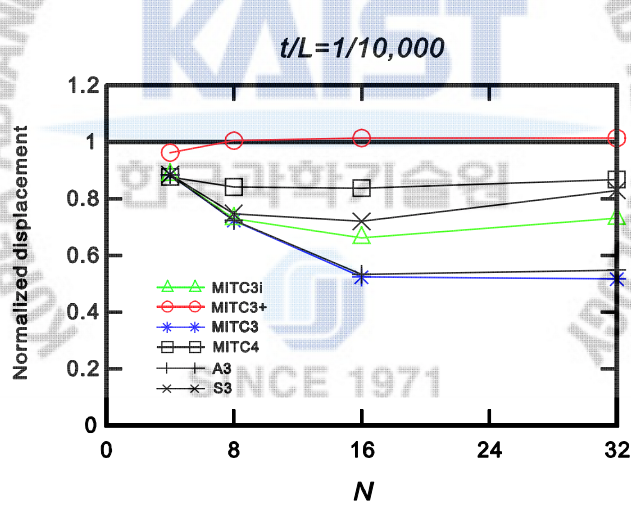
Fig. 6.5 gives the convergence curves of the normalized central displacements.  $N \times N$  element meshes ( $N = 4, 8, 16$ , and  $32$ ) are used to calculate the solutions using the shell elements. The performance of the MITC3+shell element is best among them. Even when  $t/L = 1/10,000$ , the performance of the MITC3+ is excellent while the other shell elements present some locking phenomenon.

### 6.3 Scordelis-Lo roof problem

The Scordelis-Lo roof of length  $L$ , radius  $R$  and uniform thickness  $t$  is considered as shown in Fig. 6.6. The structure is supported by rigid diagrams and loaded by gravity force (density  $\rho = 360$ ). Due to symmetry, only a one-quarter model is considered. The displacement at the middle of the free edge is 0.3024 for the reference solution [65].



(a)



(b)

Fig. 6.5 Convergence curves of the normalized central displacements ( $w_{center}$ ) for the Morley's thirty-degree skew plate problem.

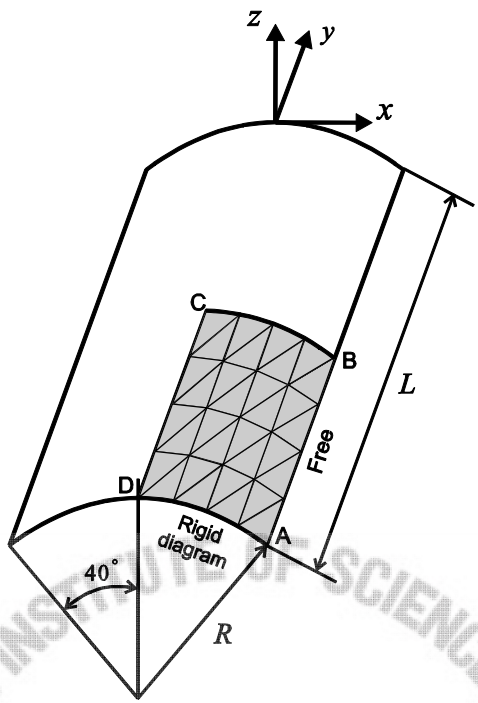


Fig. 6.6 Scordelis-Lo roof problem ( $R=25$ ,  $L=50$ ,  $t=0.25$ ,  $E=4.32 \times 10^8$  and  $\nu=0.0$ ).

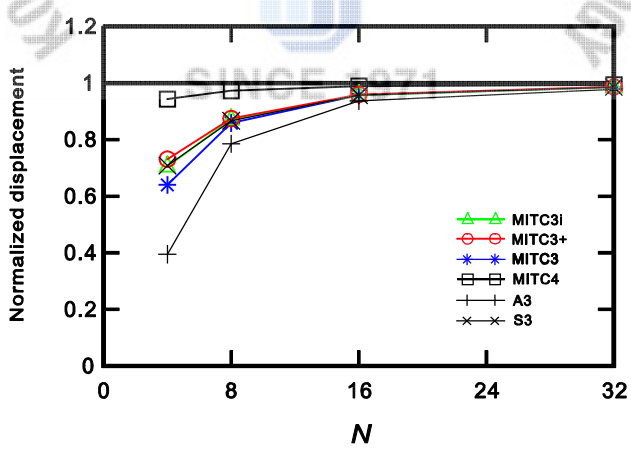


Fig. 6.7 Convergence curves of the normalized displacements ( $w_B$ ) for the Scordelis-Lo roof problem.

Fig. 6.7 presents the convergence curves of the normalized displacements ( $w_B$ ).  $N \times N$  element meshes ( $N = 4, 8, 16$ , and  $32$ ) are used to calculate the solutions using the shell elements. The performance of the MITC4 shell element is better than that of all the tested 3-node triangular shell elements.

#### 6.4 Pinched cylindrical shell problem

A pinched cylindrical shell of uniform thickness  $t$ , length  $2L$ , and radius  $R$  is considered, as seen in Fig. 6.8. Two cases are considered: a pinched cylinder with rigid diaphragms at both ends and a pinched cylinder with free ends. Due to symmetry, only a one-eighth model is considered [6,19].

Fig. 6.9 presents the convergence curves of the normalized displacements ( $w_C$ ) for the pinched cylinder with rigid diaphragms at both ends. The reference solution is  $1.8248 \times 10^{-5}$ .  $N \times N$  element meshes ( $N = 4, 8, 16$ , and  $32$ ) are used to calculate the solutions using the shell elements. The performance of the MITC3+ shell element is better than that of the other triangular shell elements. Also, the MITC3+ shell element displays the convergence behavior similar to the MITC4 shell element.

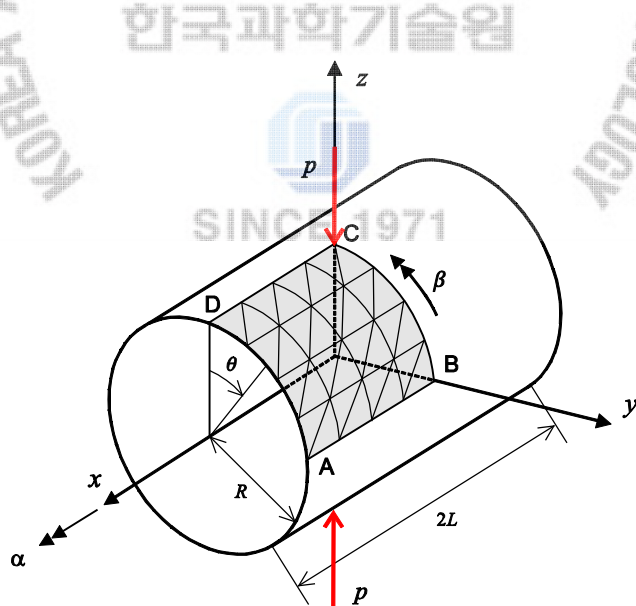


Fig. 6.8 Pinched cylindrical shell problem with the two end conditions: rigid diagrams ( $R = 1.0, L = 1.0, t = 0.01, E = 3.0 \times 10^7$  and  $\nu = 0.3$ ) and free ends ( $R = 4.953, L = 5.175, E = 10.5 \times 10^6$  and  $\nu = 0.3125$ ).

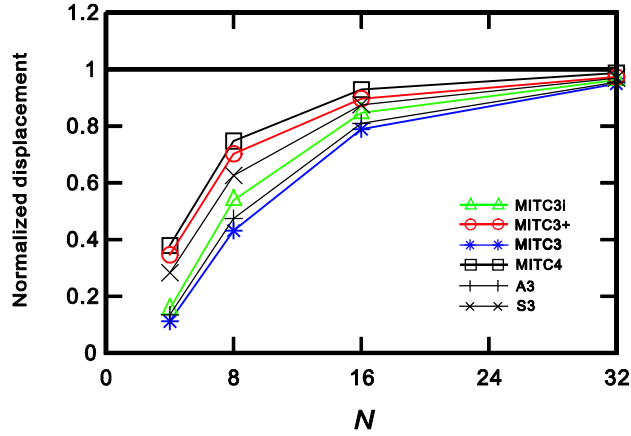


Fig. 6.9 Convergence curves of the normalized displacements ( $w_C$ ) for the pinched cylindrical shell problem with the rigid diagrams.

Fig. 6.10 presents the convergence curves of the normalized displacements ( $w_C$ ) for the pinched cylinder with free ends in two different thickness:  $t = 0.094$  and  $0.01548$ . The reference solution is  $0.1139$  when  $t = 0.094$ . The reference solution is  $0.02439$  when  $t = 0.01548$  [70]. We use  $N \times N$  element meshes ( $N = 4, 8, 16$ , and  $32$ ) to calculate the solutions using the shell elements. In these problems, all the tested shell elements present similarly good convergence behaviors.

## 6.5 Hemispherical shell problem

The hemispherical shell is considered with the uniform thickness  $t$ , radius  $R$  and  $18^\circ$  hole, as shown in Fig. 6.11. The two opposite radial concentrated force  $P$  is applied. Due to symmetry, only a one-quarter model is considered. The displacement under the applied load is  $0.094$  as the reference solution [65].

Fig. 6.12 presents the convergence curves of the normalized displacements ( $u_A$ ).  $N \times N$  element meshes ( $N = 4, 8, 16$ , and  $32$ ) are used to calculate the solutions using the shell elements. The performance of the MITC3+ shell element is much better than that of the other triangular shell elements like the MITC4 shell element.

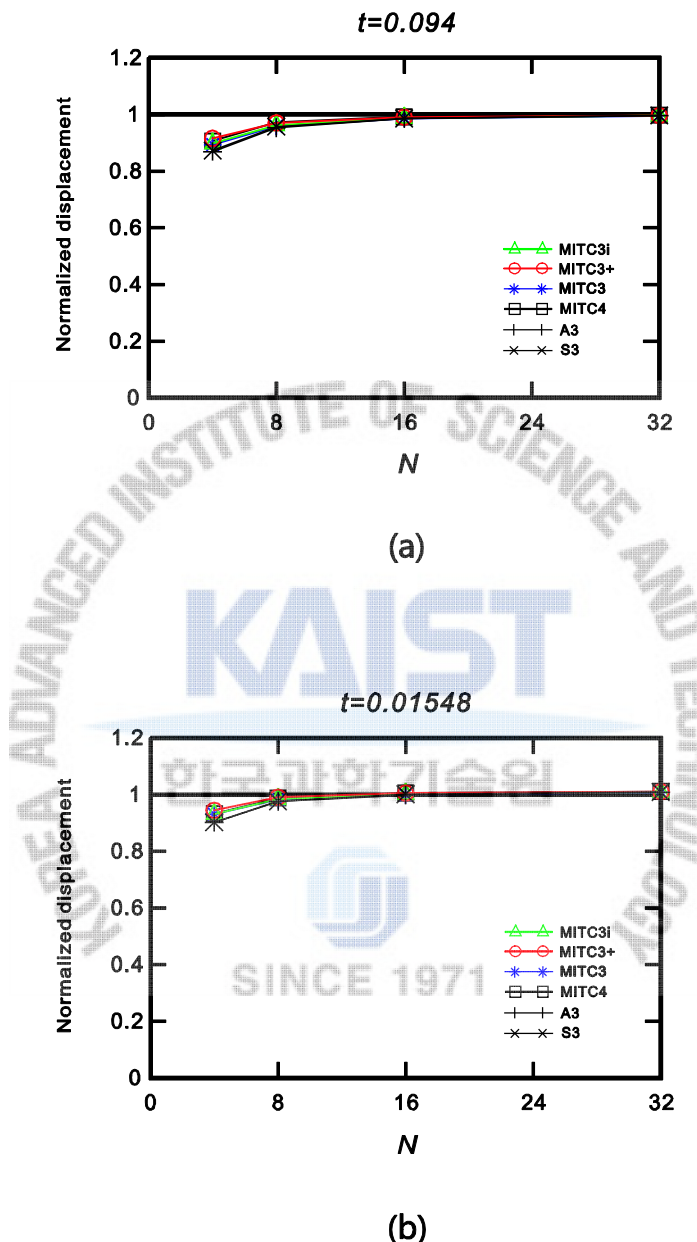


Fig. 6.10 Convergence curves of the normalized displacements ( $w_C$ ) for the pinched cylindrical shell problem with the free ends.

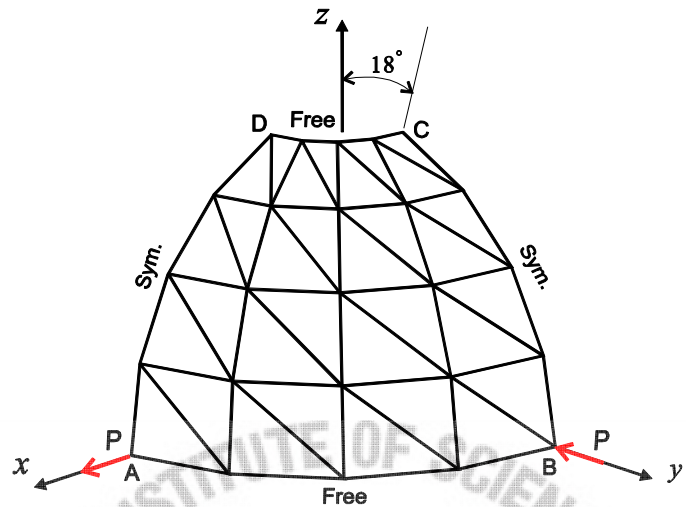


Fig. 6.11 Hemispherical shell problem ( $R=10$ ,  $t=0.04$ ,  $p=1.0$ ,  $E=6.825 \times 10^7$  and  $\nu=0.3$ ).

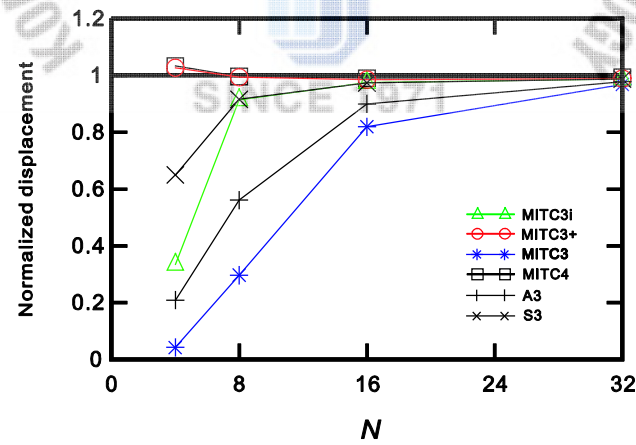


Fig. 6.12 Convergence curves of the normalized displacements ( $u_A$ ) for the hemispherical shell problem.

## 6.6 Effects of mesh distortion

In this section, the MITC3+ triangular shell element and MITC4 quadrilateral shell element are considered to study the effect of mesh distortion.

### 6.6.1 Distorted mesh A

The plate bending problem shown in Fig. 6.13 is solved using the distorted mesh A [34]. A square plate of dimensions  $L \times L$  and uniform thickness  $t$  is subjected to a uniform pressure and all the edges are fully clamped. Mesh A-1 is used for the MITC4 shell element. Mesh A-2 is used for the MITC3+ shell element.

Table 6.1 presents the strain energies calculated using the MITC4 and MITC3+ shell elements for three different thicknesses ( $t/L = 1/100, 1/1,000$  and  $1/10,000$ ). Even though the MITC4 shell element presents locking phenomenon, the MITC3+ shell element shows good results.

The quarter of an infinitely long cylinder under constant bending is also considered, see Fig. 6.14. The distorted mesh A shown in Fig 6.13 is used [34]. Table 6.2 presents the strain energies calculated using the MITC4 and MITC3+ shell elements for three different thicknesses ( $t/L = 1/100, 1/1,000$  and  $1/10,000$ ). The MITC4 shell element locks. However, the MITC3+ shell element shows much better results.

### 6.6.2 Distorted mesh B

At first, we consider the pinched cylindrical shell of uniform thickness  $t$ , length  $2L$ , and radius  $R$  with free ends, as shown in Fig. 6.8. Two different thicknesses ( $t/R = 1/100$  and  $t/R = 1/10,000$ ) are used. Due to symmetry, only a one-eighth model is considered. For the reference solution, the displacement under the applied load is given by [68]

$$w_C(P) = 0.0745 \frac{PR^3}{2DL}. \quad (6.5)$$

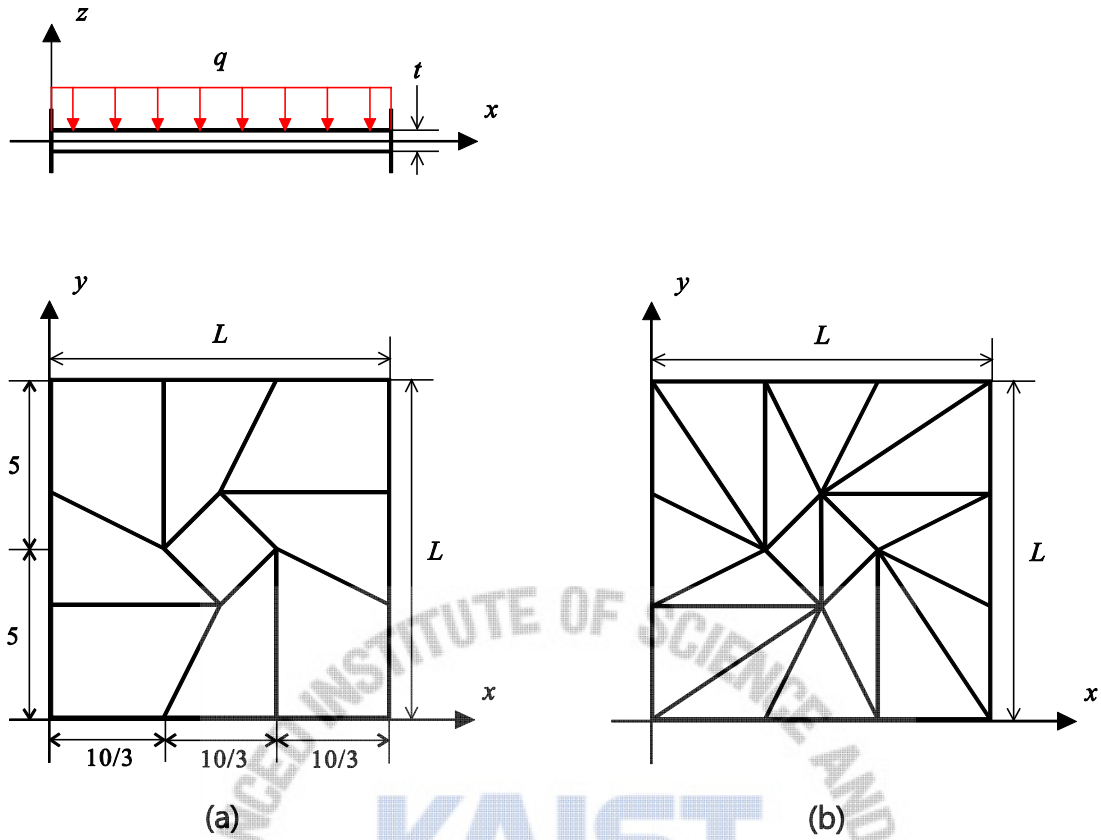


Fig. 6.13 Fully clamped square plate problem under uniform pressure ( $L = 10$ ,  $E = 1000$ ,  $q = 10$  and  $\nu = 0.3$ ).

(a) Distorted mesh A-1 for quadrilateral elements. (b) Distorted mesh A-2 for triangular elements.

The distorted mesh B shown in Fig. 6.15 is considered. Each edge is discretized by the following ratio:

$L_1 : L_2 : L_3 : \dots : L_N = 1 : 2 : 3 : \dots : N$ . Fig. 6.16 presents the convergence curves of the normalized displacements ( $w_C$ ) for the pinched cylinder with free ends using the distorted mesh. We use  $N \times N$  element meshes ( $N = 4, 8, 16$ , and  $32$ ) to calculate the solutions using the shell elements. The solution of the MITC4 shell element presents more degree of locking than that of the MITC3+ shell element. Indeed, the MITC3+ shell element shows good performance regardless of the mesh distortion.

The hemispherical shell problem shown in Fig. 6.11 is considered [65]. The distorted mesh shown Fig. 6.15 is used. Fig. 6.17 presents the convergence curves of the normalized displacements ( $u_A$ ).  $N \times N$  element meshes ( $N = 4, 8, 16$ , and  $32$ ) is used to calculate the solutions using the shell elements. The MITC3+ shell element still excellent convergence behavior even when distorted mesh.

Table 6.1 Strain energy for the fully clamped plate problem under uniform pressure with the distorted mesh shown in Fig. 6.13.

	Mesh A-1	Mesh A-2
$t/L$	MITC4	MITC3+
1/100	1.6025E+03	1.2688E+05
1/1,000	1.6186E+04	1.2616E+08
1/10,000	1.6188E+05	1.1916E+11
Order of change	$t/L$	$(t/L)^3$

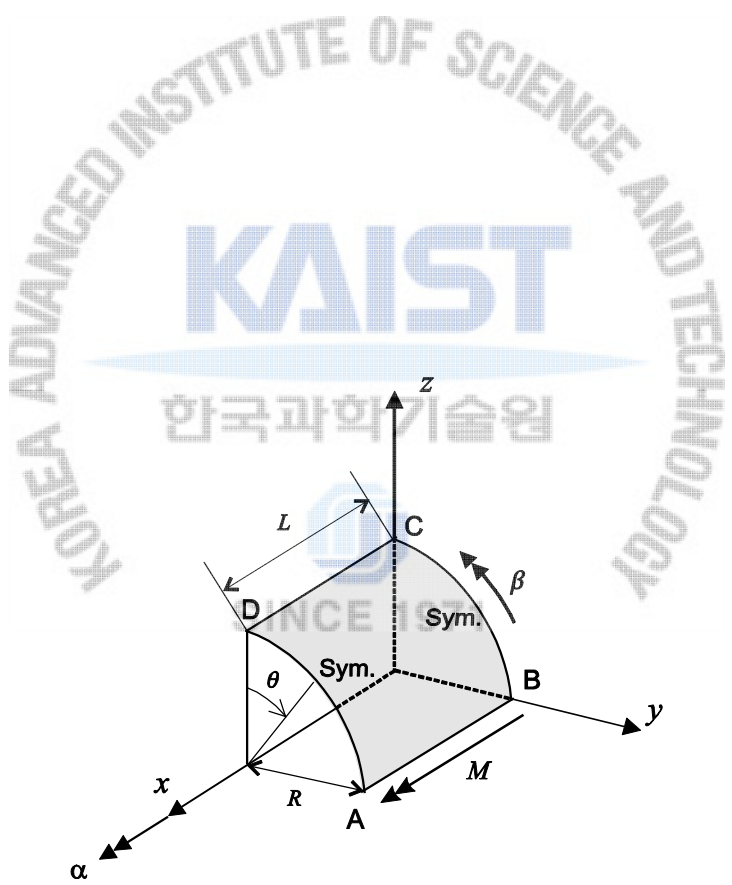


Fig. 6.14 Quarter of an infinitely long cylinder under constant bending ( $R=10$ ,  $L=10$ ,  $E=1000$  and  $\nu=0.3$ ).

Table 6.2 Strain energy for the quarter of an infinitely long cylinder with the distorted mesh shown in Fig. 6.13.

	Mesh A-1	Mesh A-2
$t/L$	MITC4	MITC3+
1/100	1.4670E+02	1.1907E+03
1/1,000	1.5935E+03	1.0070E+06
1/10,000	1.5953E+04	6.9991E+08
Order of change	$t/L$	$(t/L)^2 \sim (t/L)^3$

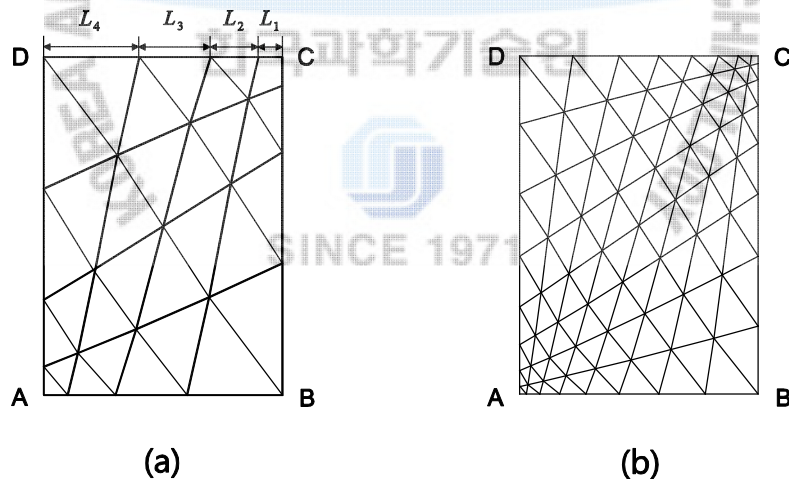
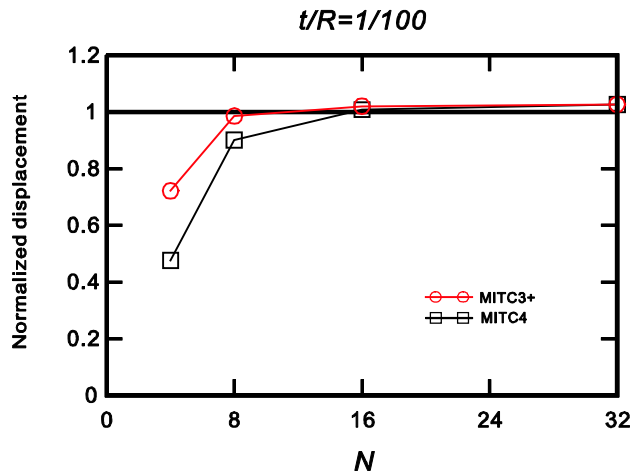
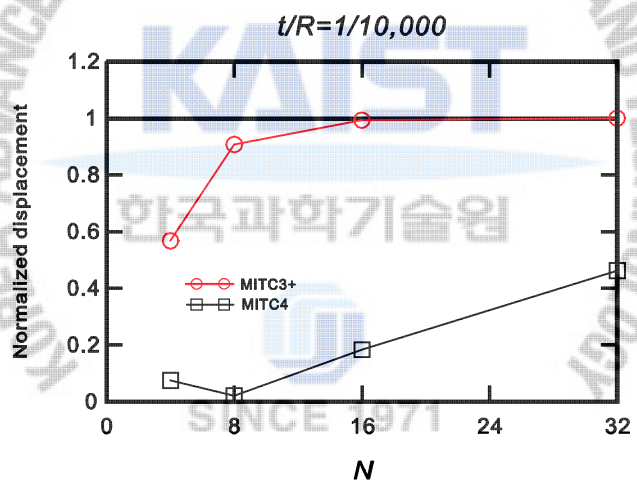


Fig. 6.15 Distorted mesh B for the cylindrical shell problem. (a) Mesh pattern used for  $N=4$ . (b) Mesh pattern used for  $N=8$ .



(a)



(b)

Fig. 6.16 Convergence curves of the normalized displacements ( $w_C$ ) for the pinched cylindrical shell problem with the free ends using the distorted meshes shown in Fig 6.15.

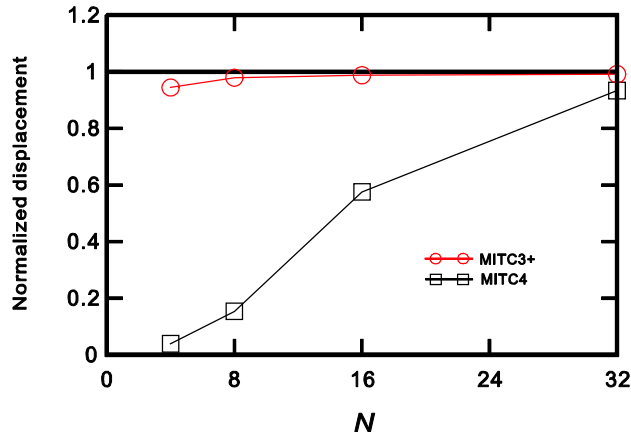
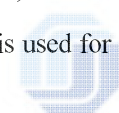


Fig. 6.17 Convergence curves of the normalized displacements ( $u_A$ ) for the hemispherical shell problem using the distorted meshes shown in Fig 6.15.

## 6.7 Closure

In the classical benchmark shell problems, the MITC3+ shell element is best among the tested 3-node shell elements. Even though the distorted mesh is used for the several benchmark shell problems, the MITC3+ shell element still shows the good results.



SINCE 1971

## Chapter7. Conclusions

The purpose of this thesis is to develop an effective 3-node continuum mechanics based triangular shell finite element in the analysis of general shell structures. Such element should present isotropic behavior and pass the consistency, ellipticity and inf-sup conditions hence and optimal in convergence tests for general shell structures.

The MITC3-HR shell finite element is developed by using the modified Hellinger-Reissner (HR) functional and by applying the proposed rotated approximated transverse shear strain field. The results of the basic numerical tests show that the MITC3-HR shell finite element satisfies all of the basic requirements. The results of the convergence studies prove that the MITC3 shell finite element is successfully improved; that is, the MITC3-HR shell finite element shows much better convergence behavior than the MITC3 shell finite element, especially in bending-dominated problems [12].

A new 3-node triangular MITC3+ shell finite element is developed for general use [24]. The MITC3+ element is based on the ‘basic mathematical shell model’ [2,45] and the MITC approach used for the development of triangular elements. The MITC3+ shell element uses a cubic bubble function for the interpolation of the rotations to enrich the bending displacement fields. The corresponding rotation degrees of freedom can be statically condensed out on the element level. A new assumed transverse shear strain field was developed with a new tying scheme to alleviate shear locking while satisfying the consistency and ellipticity conditions. The MITC3+ shell element passes the three basic tests (the patch, zero energy mode and isotropy tests) and shows excellent convergence behaviors in various shell problems even when highly distorted meshes are used[24].Excellent performance of the MITC3+ shell element in geometric nonlinear analysis was also measured [54].

Insight into the static and dynamic modal behavior of the MITC3+ triangular shell element is presented. For comparison, the pure displacement-based (DISP3), MITC3 and MITC4 shell elements are considered. Detailed static mode solutions are studied for the single right-angled triangular shell elements and the assemblage of two right-angled triangular shell elements. In the two-sided clamped plate problem, the

transverse shear strain fields of the MITC3+ shell element are investigated. Through these studies, the MITC3+ shell element formulation contains additional anti-symmetric bending modes (B1+ and B2+) due to the bubble function enrichment, and shear locking is alleviated in these modes using the MITC method. Consequently, unlike the DISP3 and MITC3 shell elements, the MITC3+ shell element performed well in the solutions of all cases.

Considering the free square problem and the free hyperboloid shell problem, dynamic mode analyses are performed. The frequencies and mode shapes are investigated. The MITC3+ shell element shows much better behaviors than the MITC3 shell element. Indeed, the MITC3+ shell element gives as accurate results as the MITC4 shell element for uniform meshes. Even when a distorted mesh is used, the MITC3+ shell element still presents good results.

In future works, firstly, it is important to develop the MITC3+ shell finite element formulation based on the large strain assumption for general shell structures [71]. Second, it is valuable to improve the membrane behavior of the MITC3+ shell element because no treatment is used for the membrane behavior [48, 49, 72, 73]. Third, the MITC3+ solid-shell element can be developed to model the three-dimensional effects of surface tractions [9]. Finally, the effectiveness of the MITC3+ shell element was demonstrated only numerically, and a mathematical analysis would be very valuable to obtain further insight into the element behavior.



## Appendix A. Mode decomposition of the 3-node plate element

The plate bending case is considered for developing the 3-node triangular plate element using the mode decomposition. The geometry and displacement interpolations in Eqs. (3.1) and (3.2) are considered. The mode decomposition method can be applied to develop other finite elements (solid, beam, shell elements, etc.).

### A.1 The MITC3 plate element

A 3-node plate element contains the 9 kinematic modes, that is, 3 rigid body modes 3 symmetrical bending modes, 1 In-plane twisting mode and 2 constant transverse shearing modes. The  $i^{\text{th}}$  kinematic modes of the 3-node plate element are defined in the Cartesian coordinates. The mode vector is considered as follows

$$\vec{\phi}_i = \{\phi_{1,i} \quad \phi_{2,i} \quad \phi_{3,i} \quad \phi_{4,i} \quad \phi_{5,i} \quad \phi_{6,i} \quad \phi_{7,i} \quad \phi_{8,i} \quad \phi_{9,i}\}^T, \quad (\text{A.1})$$

in which the components given by the nodal displacements are

$$\vec{\phi}_i = \{w_1 \quad w_2 \quad w_3 \quad \theta_x^1 \quad \theta_x^2 \quad \theta_x^3 \quad \theta_y^1 \quad \theta_y^2 \quad \theta_y^3\}^T. \quad (\text{A.2})$$

The rigid body modes ( $\vec{\phi}_1, \vec{\phi}_2, \vec{\phi}_3$ ) consist of the 1 translational and 2 rotational rigid body modes. The bending modes ( $\vec{\phi}_4, \vec{\phi}_5, \vec{\phi}_6$ ) of the arbitrary 3-node plate element are obtained from the bending axes shown in Fig. 3.4. The in-plane twisting mode( $\vec{\phi}_7$ ) shown in Fig. A.1 can be obtained by twisting about the z-axis located at the barycenter. The constant transverse shearing modes can be represented as follows

$$\vec{\phi}_8 = \{0 \quad 0 \quad 0 \quad 0 \quad 0 \quad 0 \quad 1 \quad 1 \quad 1\}^T, \quad (\text{A.3})$$

$$\vec{\phi}_9 = \{0 \quad 0 \quad 0 \quad -1 \quad -1 \quad -1 \quad 0 \quad 0 \quad 0\}^T. \quad (\text{A.4})$$

The displacement-based 3-node plate element is modified with the above mode decomposition. For the 3 bending modes, the transverse shear strain fields Eqs. (3.14)-(3.16) are imposed, respectively. The developed 3-node plate element is the same as the MITC3 plate element.

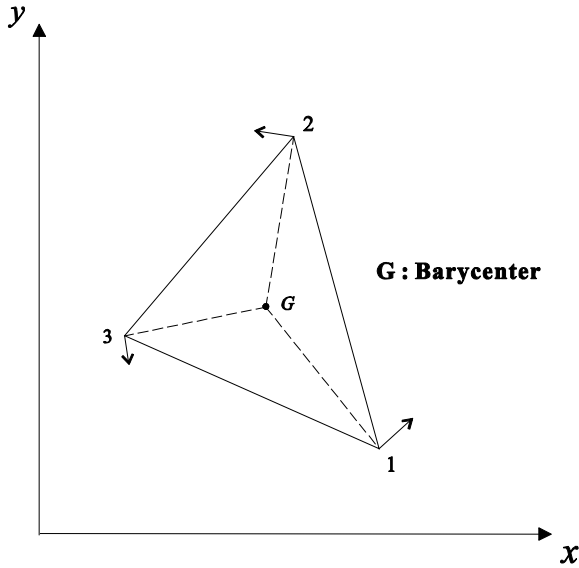


Fig. A.1 In-plane twisting mode when a single 3-node plate element is twisted at the barycenter.

#### A.2 The MITC3-MD plate element

The modes of a 3-node plate element also consist of 3 rigid body modes, 3 symmetrical bending modes and 3 antisymmetrical bending and shearing modes [6]. The antisymmetrical bending and shearing modes ( $\vec{\phi}_7$ ,  $\vec{\phi}_8$ ,  $\vec{\phi}_9$ ) of the arbitrary 3-node plate element are shown in Fig. A.2. For the 3 symmetrical bending modes, the transverse shear strain fields Eqs.(3.14)-(3.16) are imposed, respectively.

For the antisymmetrical bending and shearing mode 1 ( $\vec{\phi}_7$ ) shown in Fig. A.2(a), the assumed covariant transverse shear strain field with the tying points shown in table A.1 and Fig. A.3 is given by

$$\begin{aligned}\tilde{e}_{rt}^d &= e_{rt}^{(A)} + \frac{1}{3}c(3s-1), \\ \tilde{e}_{st}^d &= e_{st}^{(A)} + \frac{1}{3}c(1-3r),\end{aligned}\tag{A.5}$$

where  $c = (e_{rt}^{(F)} - e_{rt}^{(D)}) - (e_{st}^{(F)} - e_{st}^{(E)})$ .

For the antisymmetrical bending and shearing mode 2 ( $\vec{\phi}_8$ ) shown Fig. A.2(b), the assumed covariant transverse shear strain field with the tying points shown in table A.1 and Fig. A.3 is obtained by

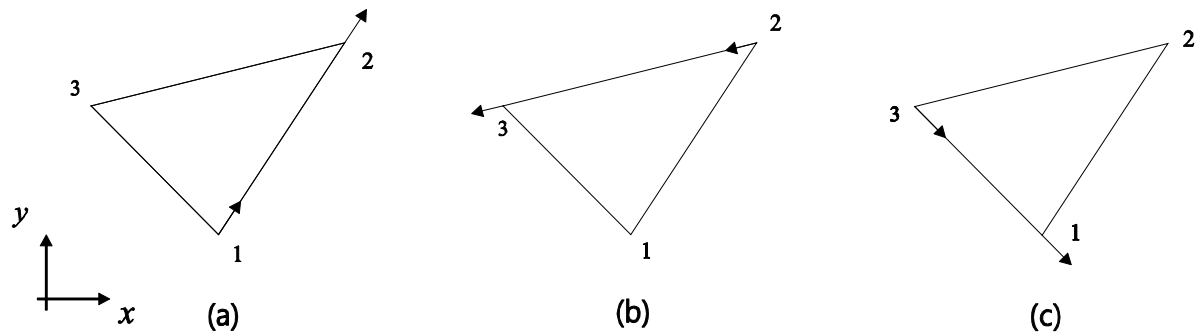


Fig. A.2 The nodal displacement pattern of the physical antisymmetrical bending and shearing strain energy modes (type A) at the top view. (a) Antisymmetrical bending and shearing mode 1. (b) Antisymmetrical bending and shearing mode 2. (c) Antisymmetrical bending and shearing mode 3.

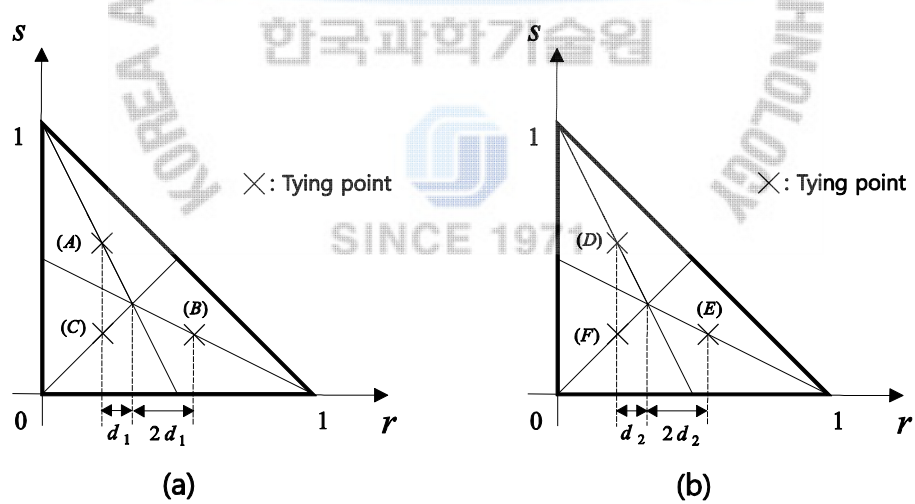


Fig. A.3 Tying positions for assumed transverse shear strain fields in the antisymmetrical bending and shearing modes.

$$\begin{aligned}\tilde{e}_{rt}^e &= e_{rt}^{(C)} + \frac{1}{3}c(3s-1), \\ \tilde{e}_{st}^e &= e_{st}^{(C)} + \frac{1}{3}c(1-3r),\end{aligned}\quad (\text{A.6})$$

where  $c = (e_{rt}^{(F)} - e_{rt}^{(D)}) - (e_{st}^{(F)} - e_{st}^{(E)})$ .

For the antisymmetrical bending and shearing mode 3 ( $\vec{\phi}_3$ ) shown Fig. A.2(c), the assumed covariant transverse shear strain field with the tying points shown in table A.1 and Fig. A.3 is given by

$$\begin{aligned}\tilde{e}_{rt}^f &= e_{rt}^{(B)} + \frac{1}{3}c(3s-1), \\ \tilde{e}_{st}^f &= e_{st}^{(B)} + \frac{1}{3}c(1-3r),\end{aligned}\quad (\text{A.7})$$

where  $c = (e_{rt}^{(F)} - e_{rt}^{(D)}) - (e_{st}^{(F)} - e_{st}^{(E)})$ .

The tying positions (A)-(F) are positioned on the three internal lines from vertices to the centers of the edges with the  $d_1$  and  $d_2$ . The  $d_1$  and  $d_2$  vary from  $2/3$  to  $-1/3$ .  $d_1$  is used  $1/12$  or  $0$ . When  $d_1$  becomes smaller, the element becomes more flexible.  $d_2 = -1/10,000$  is used to make the in-plane twisting mode more flexible without a spurious mode. This element passes the zero energy mode test, isotropic element test and the patch test except for the transverse shearing patch test.

Table A.1 Tying positions for the assumed transverse shear strain field in the antisymmetrical bending and shearing modes. The  $d_1$  and  $d_2$  are defined in Fig. A.3.

Tying positions		$r$	$s$
Fig. A.3(a)	(A)	$1/3+d_1$	$1/3-2d_1$
	(B)	$1/3-2d_1$	$1/3+d_1$
	(C)	$1/3+d_1$	$1/3+d_1$
Fig. A.3(b)	(D)	$1/3+d_2$	$1/3-2d_2$
	(E)	$1/3-2d_2$	$1/3+d_2$
	(F)	$1/3+d_2$	$1/3+d_2$

The strain energy is used for the convergence studies. The relative strain energy is defined

$$E_r = \left| \frac{E_{ref} - E_h}{E_{ref}} \right|, \quad (\text{A.8})$$

where  $E_{ref}$  is the reference of the strain energy obtained by the MITC4 plate element with  $128 \times 128$  meshes.  $E_h$  is the strain energy from the finite element solutions. Considering the fully clamped plate problem shown in Fig. 3.12, the convergence curves are presented in Fig. A.4. The MITC3-MD element presents the improved performance compared with the MITC3 element. If the antisymmetrical bending and shearing modes shown in Fig. A.5 are used with  $d_1 = 1/12$ , the element passes all the basic tests. The performance is similar to the MITC3-HR element.

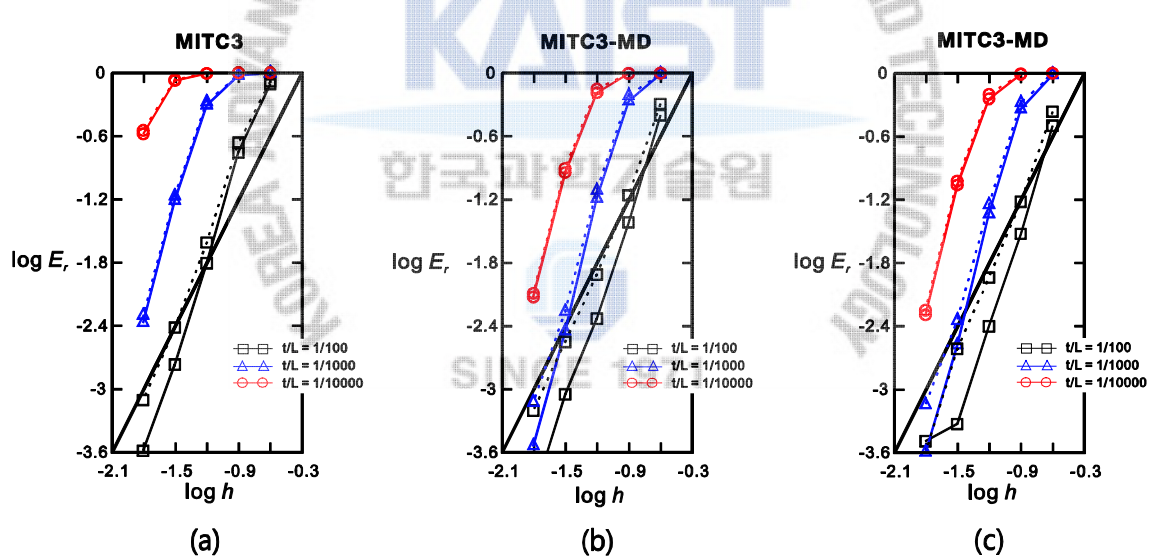


Fig. A.4 Convergence curves for the fully clamped square plate problem. The bold line represents the optimal convergence rate. The solid and dotted lines correspond to the results obtained by the mesh patterns in Figs. 3.12(a) and (b), respectively. (a) MITC3 element. (b) MITC3-MD element ( $d_1 = 1/12$ ). (c) MITC3-MD element ( $d_1 = 0$ ).

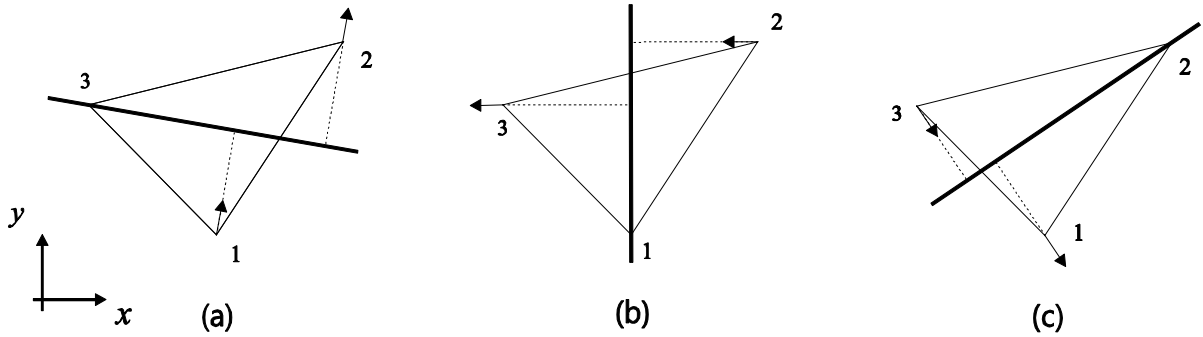


Fig. A.5 The nodal displacement pattern of the physical antisymmetrical bending and shearing strain energy modes (type B) at the top view. (a) Antisymmetrical bending and shearing mode 1. (b) Antisymmetrical bending and shearing mode 2. (c) Antisymmetrical bending and shearing mode 3.

From these studies, it is revealed that when developing a standard 3-node shell finite element in which the geometry and displacement interpolations in Eqs. (3.1) and (3.2), the 3-node shell finite element that passes all the basic tests (the zero energy mode test, the patch test, and the isotropic element test) has limitation to obtain the excellent results in convergence tests like the 4-node shell element (MITC4). Fundamentally, the 3-node shell element lacks bending displacements. The 3-node shell element cannot properly represent the antisymmetrical bending modes, that is, the higher order bending modes. In the plate bending problems, when using the higher-order triangular shell element that the antisymmetrical bending modes can be represented properly, the convergence behavior is excellent [10, 23]. Hence, to improve the performance of the 3-node shell element as good as that of the 4-node shell element, the shape functions should be enriched to represent the antisymmetrical bending modes suitably [10, 23, 46-48].

## Appendix B. Assumed transverse shear strain fields for a 3-node shell element

New assumed transverse shear strain fields are designed using the new tying scheme. The 3-node shell elements are developed using the new assumed transverse shear strain fields.

First, the nine covariant transverse shear strains shown in Fig. B.1 are defined as follows

$$\tilde{e}_{1t}^A = -\frac{1}{\sqrt{17}}(4\tilde{e}_{st} + \tilde{e}_{rt}), \quad \tilde{e}_{2t}^A = \frac{1}{\sqrt{26}}(5\tilde{e}_{st} - \tilde{e}_{rt}), \quad \tilde{e}_{3t}^A = \tilde{e}_{2t} = \frac{2\sqrt{5}}{5}\left(-\frac{1}{2}\tilde{e}_{st} + \tilde{e}_{rt}\right), \quad (\text{B.1})$$

$$\tilde{e}_{1t}^B = \frac{1}{\sqrt{26}}(-\tilde{e}_{st} + 5\tilde{e}_{rt}), \quad \tilde{e}_{2t}^B = -\frac{1}{\sqrt{17}}(\tilde{e}_{st} + 4\tilde{e}_{rt}), \quad \tilde{e}_{3t}^B = \tilde{e}_{1t} = \frac{2\sqrt{5}}{5}\left(\tilde{e}_{st} - \frac{1}{2}\tilde{e}_{rt}\right), \quad (\text{B.2})$$

$$\tilde{e}_{1t}^C = \frac{1}{\sqrt{41}}(5\tilde{e}_{st} - 4\tilde{e}_{rt}), \quad \tilde{e}_{2t}^C = \frac{1}{\sqrt{41}}(-4\tilde{e}_{st} + 5\tilde{e}_{rt}), \quad \tilde{e}_{3t}^C = \tilde{e}_{3t} = -\frac{1}{\sqrt{2}}(\tilde{e}_{st} + \tilde{e}_{rt}). \quad (\text{B.3})$$

The transverse shear strain components are sampled at nine internal tying points (1)-(9) on the nine internal lines, see Fig. B.2(a) and Table B.1. The constant covariant transverse shear strains along the element edge directions are assumed to be

$$\begin{aligned} \tilde{e}_{rt}(0,0) &= \tilde{e}_{rt}(1,0) = \frac{1}{3}\left(-\frac{1}{2}e_{st}^{(7)} + e_{rt}^{(7)}\right) + \frac{1}{18}(e_{st}^{(6)} + 4e_{rt}^{(6)}) + \frac{1}{6}(e_{st}^{(4)} + e_{rt}^{(4)}) + \frac{1}{18}(-e_{st}^{(5)} + 5e_{rt}^{(5)}), \\ \tilde{e}_{st}(0,0) &= \tilde{e}_{st}(0,1) = \frac{1}{3}(e_{st}^{(1)} - \frac{1}{2}e_{rt}^{(1)}) + \frac{1}{18}(4e_{st}^{(2)} + e_{rt}^{(2)}) + \frac{1}{6}(e_{st}^{(4)} + e_{rt}^{(4)}) + \frac{1}{18}(5e_{st}^{(3)} - e_{rt}^{(3)}), \\ \tilde{e}_{st}(1,0) &= \tilde{e}_{st}(0,1) = \frac{1}{\sqrt{2}}\left(\frac{1}{3}(e_{st}^{(1)} - \frac{1}{2}e_{rt}^{(1)}) - \frac{1}{18}(-4e_{st}^{(9)} + 5e_{rt}^{(9)}) - \frac{1}{3}(-\frac{1}{2}e_{st}^{(7)} + e_{rt}^{(7)}) + \frac{1}{18}(5e_{st}^{(8)} - 4e_{rt}^{(8)})\right). \end{aligned} \quad (\text{B.4})$$

The conditions in Eq. (B.4) is imposed to the interpolation in Eq. (3.11) to obtain the unknown coefficients. Finally, the assumed covariant transverse shear strain field (Type A) is given by

$$\begin{aligned} \tilde{e}_{rt} &= \frac{1}{3}\left(-\frac{1}{2}e_{st}^{(7)} + e_{rt}^{(7)}\right) + \frac{1}{18}(e_{st}^{(6)} + 4e_{rt}^{(6)}) + \frac{1}{6}(e_{st}^{(4)} + e_{rt}^{(4)}) + \frac{1}{18}(-e_{st}^{(5)} + 5e_{rt}^{(5)}) + Cs \\ \tilde{e}_{st} &= \frac{1}{3}(e_{st}^{(1)} - \frac{1}{2}e_{rt}^{(1)}) + \frac{1}{18}(4e_{st}^{(2)} + e_{rt}^{(2)}) + \frac{1}{6}(e_{st}^{(4)} + e_{rt}^{(4)}) + \frac{1}{18}(5e_{st}^{(3)} - e_{rt}^{(3)}) - Cr \end{aligned} \quad (\text{B.5})$$

where  $C = \frac{1}{18}(4e_{st}^{(2)} + e_{rt}^{(2)} + 5e_{st}^{(3)} - e_{rt}^{(3)} + e_{st}^{(5)} - 5e_{rt}^{(5)} - e_{st}^{(6)} - 4e_{rt}^{(6)} - 5e_{st}^{(8)} + 4e_{rt}^{(8)} - 4e_{st}^{(9)} + 5e_{rt}^{(9)})$ .

The 3-node shell finite element in which the geometry and displacement interpolations in Eqs. (3.1) and (3.2) and is developed with the new assumed transverse shear strain field in Eq. (B.5). We label the MITC3i-a element. The element passes all the basic tests.

Also, the transverse shear strain components are sampled at six internal tying points (1)-(6) on the six internal lines, see Fig. B.2(b) and Table B.1. The constant covariant transverse shear strains along the element edge directions are assumed to be

$$\tilde{e}_{rt}(0,0) = \tilde{e}_{rt}(1,0) = \frac{1}{9}(-e_{st}^{(l)} + 5e_{rt}^{(l)}) + \frac{1}{9}(e_{st}^{(k)} + 4e_{rt}^{(k)}),$$

$$\tilde{e}_{st}(0,0) = \tilde{e}_{st}(0,1) = \frac{1}{9}(5e_{st}^{(i)} - e_{rt}^{(i)}) + \frac{1}{9}(4e_{st}^{(j)} + e_{rt}^{(j)}), \quad (B.6)$$

$$\tilde{e}_{qt}(1,0) = \tilde{e}_{qt}(0,1) = \frac{1}{\sqrt{2}}\left(\frac{1}{9}(5e_{st}^{(n)} - 4e_{rt}^{(n)}) - \frac{1}{9}(-4e_{st}^{(m)} + 5e_{rt}^{(m)})\right).$$

The conditions in Eq. (B.6) is imposed to the interpolation in Eq. (3.11) to obtain the unknown coefficients. The assumed covariant transverse shear strain field (Type B) is obtained by

$$\begin{aligned} \tilde{e}_{rt} &= \frac{1}{9}(-e_{st}^{(l)} + 5e_{rt}^{(l)}) + \frac{1}{9}(e_{st}^{(k)} + 4e_{rt}^{(k)}) + Ms \\ \tilde{e}_{st} &= \frac{1}{9}(5e_{st}^{(i)} - e_{rt}^{(i)}) + \frac{1}{9}(4e_{st}^{(j)} + e_{rt}^{(j)}) - Mr \end{aligned} \quad (B.7)$$

$$\text{where } M = \frac{1}{9}(5e_{st}^{(i)} - e_{rt}^{(i)} + 4e_{st}^{(j)} + e_{rt}^{(j)} - e_{st}^{(k)} - 4e_{rt}^{(k)} + e_{st}^{(l)} - 4e_{rt}^{(l)} - 5e_{st}^{(m)} + 5e_{rt}^{(m)} - 5e_{st}^{(n)} + 4e_{rt}^{(n)}).$$

The 3-node shell finite element where the geometry and displacement interpolations in Eqs. (3.1) and (3.2) is developed with the new assumed transverse shear strain field in Eq. (B.7). We label the MITC3i-b element. The element passes all the basic tests.

The fully clamped problem shown in Fig. 3.12, the cylindrical shell problems shown in Fig. 3.18 and the hyperboloid shell problems shown in Fig. 3.23 in Section 3.3 are considered for convergence tests of the MITC3i-a and MITC3i-b elements. Using the s-norm, the convergence curves are shown in Figs.B.3-B.7 for above benchmark shell problems, respectively. In the bending-dominated problems, the performance of the MITC3i-a and MITC3i-b shell elements is improved compared to the MITC3 shell element. However, the performance of the MITC3i shell element is better than that of two developed shell elements because the MITC3i shell element contains the more flexible in-plane twisting mode, see the convergence curves for the MITC3i element in section 4.4.

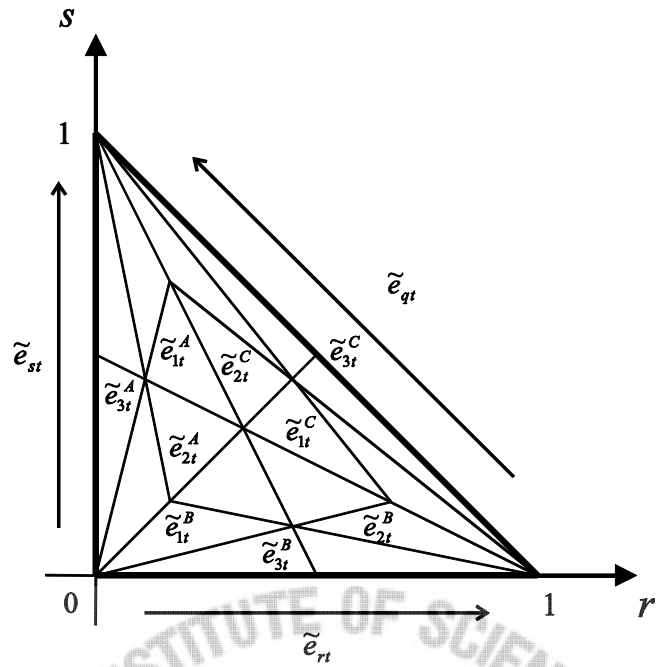


Fig. B.1 Transverse shear strains.

Table B.1 Tying positions for the assumed transverse shear strain fields for the MITC3i-a and MITC3i-b shell elements.

	Tying positions	$r$	$s$
Fig. B.2(a)	(1)	1 / 12	5 / 6
	(2)	5 / 36	5 / 9
	(3)	5 / 36	11 / 36
	(4)	1 / 12	1 / 12
	(5)	11 / 36	5 / 36
	(6)	5 / 9	5 / 36
	(7)	5 / 6	1 / 12
	(8)	5 / 9	11 / 36
	(9)	11 / 36	5 / 9
Fig. B.2(b)	(i)	1 / 18	13 / 18
	(j)	1 / 18	4 / 18
	(k)	4 / 18	1 / 18
	(l)	13 / 18	1 / 18
	(m)	13 / 18	4 / 18
	(n)	4 / 18	13 / 18

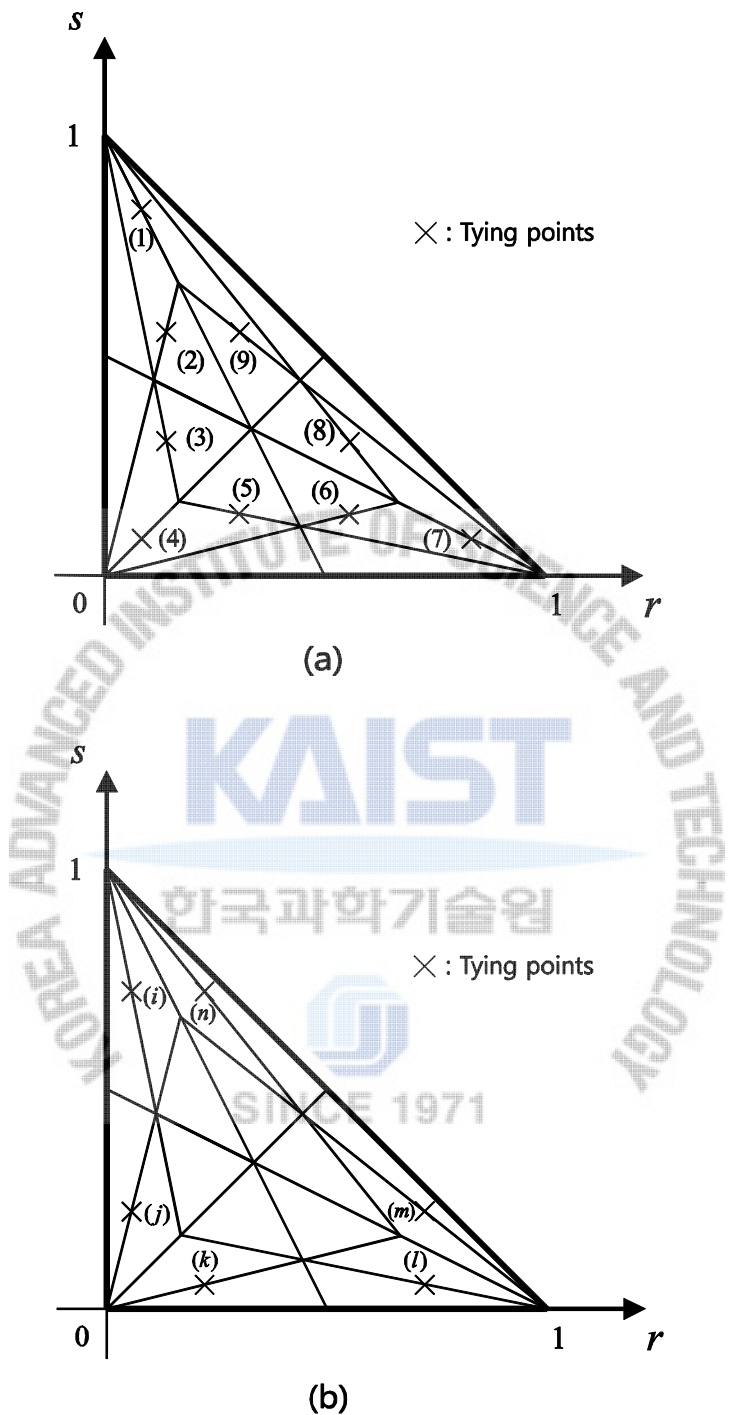


Fig. B.2 Tying positions for the assumed transverse shear strain field. (a) Type A. (b) Type B.

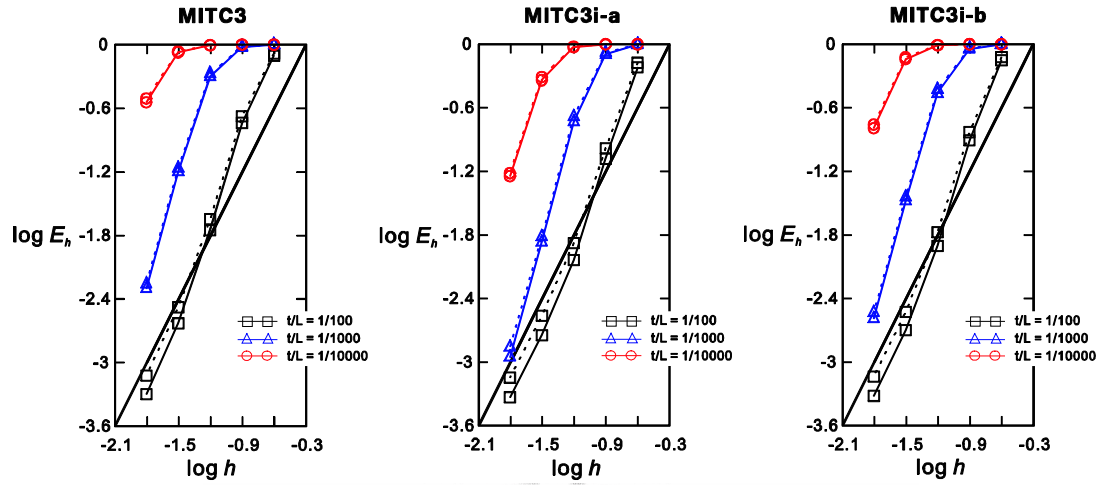


Fig. B.3 Convergence curves for the fully clamped square plate problem. The bold line represents the optimal convergence rate. The solid and dotted lines correspond to the results obtained by the mesh patterns in Figs. 3.12(a) and (b), respectively.

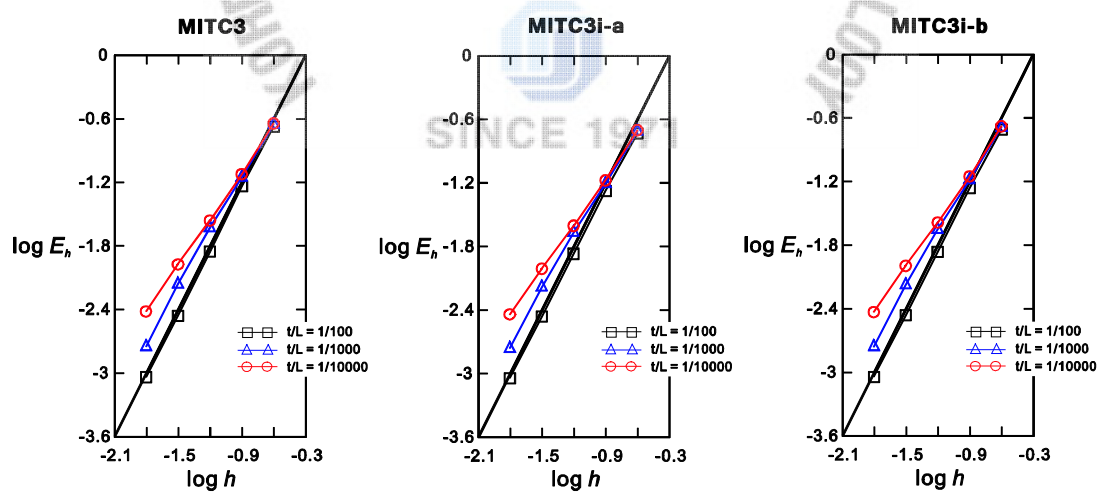


Fig. B.4 Convergence curves for the clamped cylindrical shell problem. The bold line represents the optimal convergence rate.

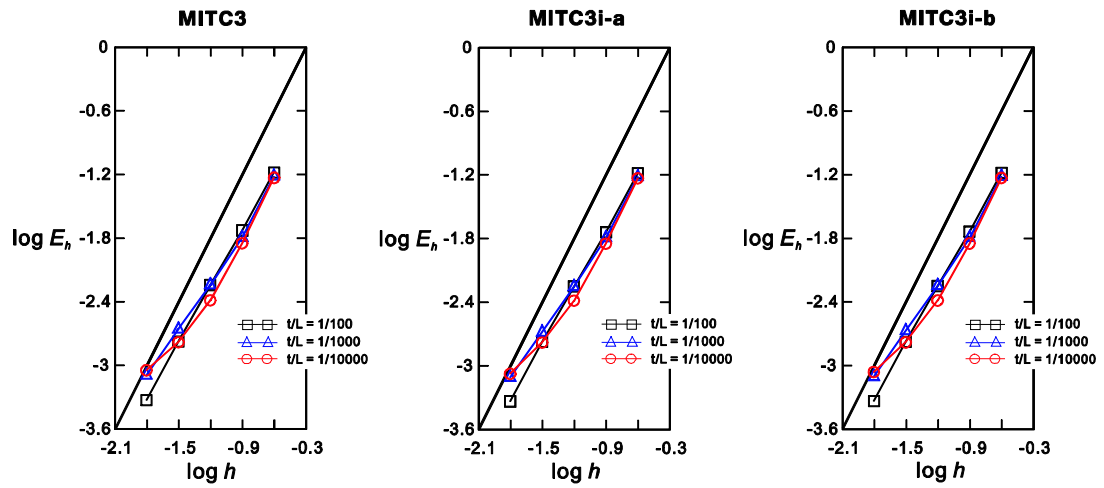


Fig. B.5 Convergence curves for the free cylindrical shell problem. The bold line represents the optimal convergence rate.

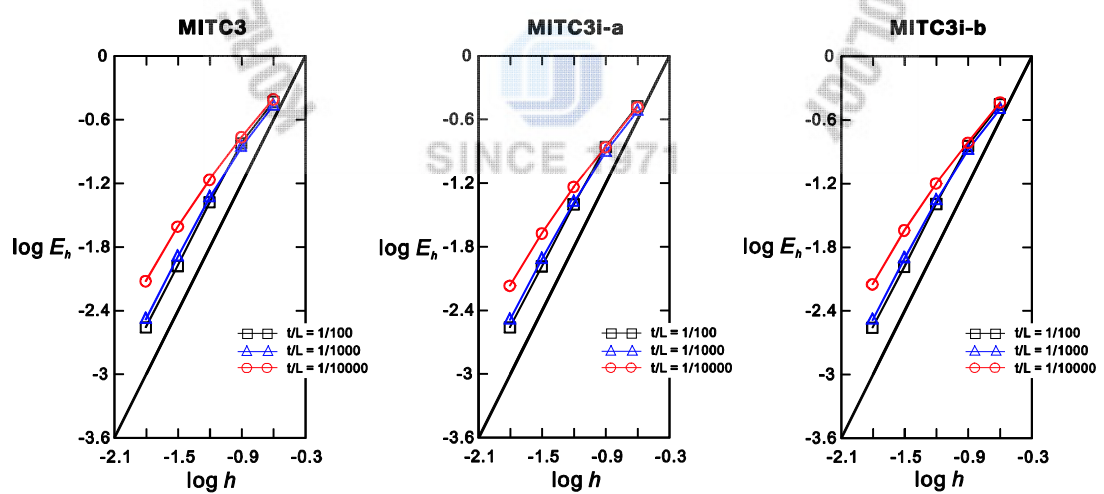


Fig. B.6 Convergence curves for the clamped hyperboloid shell problem. The bold line represents the optimal convergence rate.

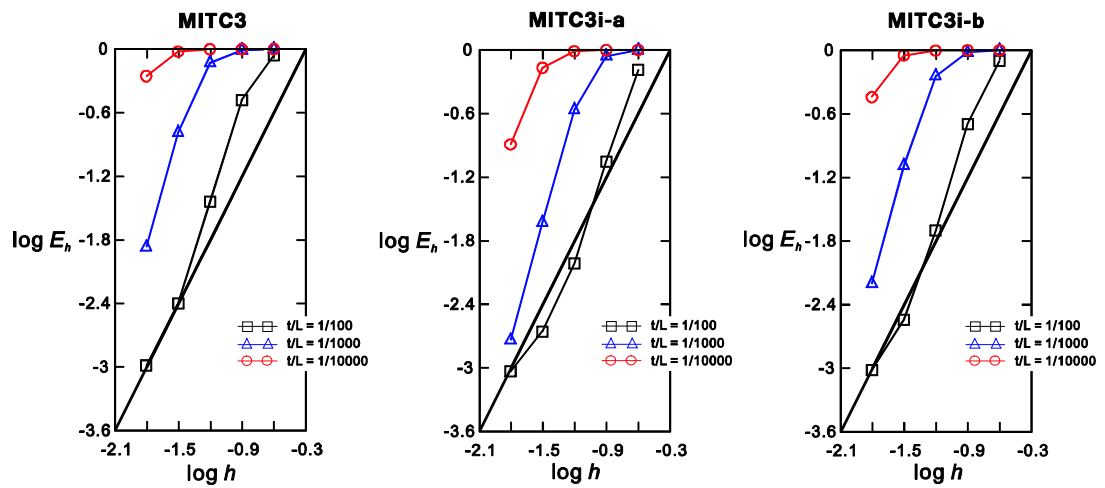


Fig. B.7 Convergence curves for the free hyperboloid shell problem. The bold line represents the optimal convergence rate.

**KAIST**

한국과학기술원



SINCE 1971

## Appendix C. Transverse shear strain fields of the MITC3+ element in flat geometry

The shell finite element can be used for plate bending problems with the following assumption when the geometry is defined on the XY-plane with constant thickness [11]

$$\vec{x}_i = \begin{Bmatrix} x_i \\ y_i \\ 0 \end{Bmatrix}, \quad \vec{u}_i = \begin{Bmatrix} 0 \\ 0 \\ w_i \end{Bmatrix}, \quad \vec{V}_n^i = \vec{i}_z, \quad \vec{V}_1^i = \vec{i}_x, \quad \vec{V}_2^i = \vec{i}_y \quad \text{and} \quad a_i = a \quad \text{for all } i, \quad (\text{C.1})$$

where  $\vec{i}_x$ ,  $\vec{i}_y$  and  $\vec{i}_z$  are the unit base vectors in the global Cartesian coordinate system.

From Eqs. (5.1)-(5.3), the geometry and displacement interpolations of the MITC3+ shell element are given with the conditions in Eq. (C.1)

$$\vec{x} = \begin{Bmatrix} \sum_{i=1}^3 h_i x_i \\ \sum_{i=1}^3 h_i y_i \\ \frac{t}{2} a \end{Bmatrix}, \quad \vec{u} = \begin{Bmatrix} \frac{t}{2} a \sum_{i=1}^4 f_i \beta_i \\ -\frac{t}{2} a \sum_{i=1}^4 f_i \alpha_i \\ \sum_{i=1}^3 h_i w_i \end{Bmatrix}. \quad (\text{C.2})$$

Using Eq. (5.9) and (C.2), the transverse shear strain field of the MITC3+ element is given by

$$\hat{e}_{rt}^{MITC3+} = \frac{a}{4} \left[ w_2 - w_1 + \frac{1}{6} (x_2 - 2x_1 + x_3) \beta_1 + \frac{1}{6} (2x_2 - x_1 - x_3) \beta_2 + \frac{1}{2} (x_2 - x_1) \beta_4 \right.$$

$$\left. + \frac{1}{6} (2y_1 - y_2 - y_3) \alpha_1 + \frac{1}{6} (y_1 - 2y_2 + y_3) \alpha_2 + \frac{1}{2} (y_1 - y_2) \alpha_4 \right] + \frac{1}{3} \hat{c} (3s - 1),$$

$$\hat{e}_{st}^{MITC3+} = \frac{a}{4} \left[ w_3 - w_1 + \frac{1}{6} (x_3 + x_2 - 2x_1) \beta_1 + \frac{1}{6} (2x_3 - x_2 - x_1) \beta_3 + \frac{1}{2} (x_3 - x_1) \beta_4 \right.$$

$$\left. + \frac{1}{6} (2y_1 - y_2 - y_3) \alpha_1 + \frac{1}{6} (y_1 + y_2 - 2y_3) \alpha_3 + \frac{1}{2} (y_1 - y_3) \alpha_4 \right] + \frac{1}{3} \hat{c} (1 - 3r), \quad (\text{C.3})$$

with

$$\begin{aligned} \hat{c} = & \frac{3}{4} ad [(y_2 - y_3) \alpha_1 + (y_3 - y_1) \alpha_2 + (y_1 - y_2) \alpha_3 \\ & + (x_3 - x_2) \beta_1 + (x_1 - x_3) \beta_2 + (x_2 - x_1) \beta_3]. \end{aligned} \quad (\text{C.4})$$

## References

- [1] Bathe KJ. Finite element procedures. New York: Prentice Hall; 1996.
- [2] Chapelle D, Bathe KJ. The finite element analysis of shells - fundamentals. Second Edition. Berlin: Springer-Verlag; 2011.
- [3] Batoz JL, Bathe KJ, Ho LW. A study of three-node triangular plate bending elements. International Journal for Numerical Methods in Engineering 1980;15:1771-1812.
- [4] Felippa CA, Bergan PG. A triangular bending element based on an energy-orthogonal free formulation. Computer Methods in Applied Mechanics and Engineering 1987;61:129-160.
- [5] Bletzinger KU, Bischoff M, Ramm E. A unified approach for shear-locking-free triangular and rectangular shell finite elements. Computers and Structures2000;75:321-334.
- [6] Argyris JH, Papadrakakis M, Apostolopoulou C, Koutsourelakis S. The TRIC shell element: theoretical and numerical investigation. Computer Methods in Applied Mechanics and Engineering 2000;182:217-245.
- [7] Park KC, Stanley GM. A curved  $C^0$  Shell Element Based on Assumed Natural-Coordinate Strains. Journal of applied Mechanics 1986;53:278-290.
- [8] Lee PS, Bathe KJ. Insight into finite element shell discretizations by use of the “basic shell mathematical model.” Computers and Structures2005;83:69-90.
- [9] Kim DN, Bathe KJ. A 4-node 3D-shell element to model shell surface tractions and incompressible behavior. Computers and Structures2008;86:2027-2041.

- [10] Lee PS, Bathe KJ. Development of MITC isotropic triangular shell finite elements. Computers and Structures 2004;82:945-962.
- [11] Lee PS, Noh HC, Bathe KJ. Insight into 3-node triangular shell finite elements : the effects of element isotropy and mesh patterns. Computers and Structures 2007;85:404-418.
- [12] Lee Y, Yoon K, Lee PS, Improving the MITC3 shell finite element by using the Hellinger-Reissner principle. Computers and Structures 2012;110-111:93-106.
- [13] Bathe KJ, Lee PS. Measuring the convergence behavior of shell analysis schemes. Computers and Structures 2011;89:285-301.
- [14] Chapelle D, Bathe KJ. Fundamental considerations for finite element analysis of shell structures. Computers and Structures 1998;66:19-36, 711-712.
- [15] Baiocchi C, Lovadina C. A shell classification by interpolation. Mathematical Models and Methods in Applied Sciences 2002;12(10):1359-1380.
- [16] Lee PS, Bathe KJ. On the asymptotic behavior of shell structures and the evaluation in finite element solutions. Computers and Structures 2002;80:235-255.
- [17] Beirão da Veiga L. Asymptotic energy behavior of two classical intermediate benchmark shell problems. Mathematical Models and Methods in Applied Sciences 2003;13:1279-1302.
- [18] Bathe KJ, Chapelle D, Lee PS. A shell problem 'highly sensitive' to thickness changes. International Journal for Numerical Methods in Engineering 2003;57:1039-1052.
- [19] Dvorkin EN, Bathe KJ. A continuum mechanics based four-node shell element for general nonlinear analysis. Engineering Computations 1984;1:77-88.
- [20] Bathe KJ, Dvorkin EN. A formulation of general shell elements - the use of mixed interpolation of tensorial components. International Journal for Numerical Methods in Engineering 1986;22:697-722.

- [21] Bucalem ML, Bathe KJ. Higher-order MITC general shell elements. International Journal for Numerical Methods in Engineering 1993;36:3729-3754.
- [22] Bathe KJ, Lee PS, Hiller JF. Towards improving the MITC9 shell element. Computers and Structures 2003;81:477-489.
- [23] Kim DN, Bathe KJ. A triangular six-node shell element. Computers and Structures 2009;87:1451-1460.
- [24] Lee Y, Lee PS, Bathe KJ. The MITC3+ shell element and its performance. Computers and Structures 2014;138:12-23.
- [25] Lee Y, Jeon HM, Lee PS, Bathe KJ. The modal behavior of the MITC3+ shell triangular shell element, submitted in *Computers and Structures*.
- [26] Lee PS, Noh HC. On the finite element analysis of shell structures (쉘구조물의 유한요소해석에 대하여). Journal of KSCE 2007;27:277-289.
- [27] Ahmad S, Irons BM, Zienkiewicz OC. Analysis of thick and thin shell structures by curved finite elements. International Journal for Numerical Methods in Engineering 1970;2;419-451.
- [28] Zienkiewicz OC, Taylor RL, Too JM. Reduced integration technique in general analysis of plates and shells. International Journal for Numerical Methods in Engineering 1971;3:275-290.
- [29] Hughes TJR, Cohen M, Haroun M. Reduced and selective integration techniques in the finite element analysis of plates. Nuclear Engineering and Design 1978;46:203-222.
- [30] Belytschko T, Tsay CS. A stabilization procedure for the quadrilateral plate element with one-point quadrature. International Journal for Numerical Methods in Engineering 1983;19:405-419.

- [31] Simo JC, Rifai MS. A class of mixed assumed strain methods and the method of incompatible modes. International Journal for Numerical Methods in Engineering 1990;29:1595-1638.
- [32] Simo JC, Armero F. Geometrically non-linear enhanced strain mixed methods and the method of incompatible modes. International Journal for Numerical Methods in Engineering 1992;33:1413-1449.
- [33] Simo JC, Armero F, Taylor RL. Improved versions of assumed enhanced strain-tri-linear elements for 3D finite deformation problems. Computer Methods in Applied Mechanics and Engineering 1993;110:359-386.
- [34] Andelfinger U, Ramm E. EAS-elements for two-dimensional, three-dimensional, plate and shell structures and their equivalence to HR-elements. International Journal for Numerical Methods in Engineering 1993;36:1311-1337.
- [35] To CWS, Liu ML. Hybrid strain based three-node flat triangular shell finite elements. Finite Element in Analysis and Design 1994;17:169-203.
- [36] Rhee JJ, Lee SW. A new efficient mixed formulation for thin shell finite element models. International Journal for Numerical Methods in Engineering 1987;24:581-604.
- [37] MacNeal RH. Derivation of element stiffness matrices by assumed stress distributions. Nuclear Engineering and Design 1982;70:3-12.
- [38] Hughes TJR. Finite elements based upon Mindlin plate theory with particular reference to the four-node bilinear isoparametric element. Journal of Applied Mechanics 1981;48:587-596.
- [39] Bathe KJ, Iosilevich A, Chapelle D. An evaluation of the MITC shell elements. Computers and Structures 2000;75:1-30.
- [40] Lee PS, Bathe KJ. The quadratic MITC plate and MITC shell elements in plate bending. Advances in Engineering Software 2010;41:712-728.

- [41] Hiller JF, Bathe KJ. Measuring convergence of mixed finite element discretizations: an application to shell structures. *Computers and Structures* 2003;81:639-654.
- [42] Bathe KJ, Iosilevich A, Chapelle D. An inf-sup test for shell finite elements. *Computers and Structures* 2000;75:439-456.
- [43] Bathe KJ. The inf-sup condition and its evaluation for mixed finite element methods. *Computers and Structures* 2001;79:243-252, 971.
- [44] Bathe KJ, Brezzi F, Marini LD. The MTC9 shell element in plate bending: mathematical analysis of a simplified case. *Computational Mechanics* 2011; 47: 617-626.
- [45] Chapelle D, Bathe KJ. The mathematical shell model underlying general shell elements. *International Journal for Numerical Methods in Engineering* 2000;48:289-313.
- [46] Wilson EL, Ibrahimbegovic A. Use of incompatible displacement modes for the calculation of element stiffness or stresses. *Finite Elements in Analysis Design* 1990;7:229-241.
- [47] Arnold DN, Brezzi F, Fortin M. A stable finite element for the Stokes equations. *Estratto da Calcolo* 1984; 21:337-344.
- [48] Kim J, Bathe KJ. The finite element method enriched by interpolation covers. *Computers and Structures* 2013;116:35-46.
- [49] Jeon HM, Lee PS, Bathe KJ. The MITC3 shell finite element enriched by interpolation covers. *Computers and Structures* 2014;134:128-142.
- [50] Kohno H, Bathe KJ. A flow-condition-based interpolation finite element procedure for triangular grids. *International Journal for Numerical Methods in Fluids* 2006;51:673-699.

- [51] Pinsky PM, Jasti RV. A mixed finite element formulation for Reissner-Mindlin plates based on the use of bubble functions. International Journal for Numerical Methods in Engineering 1989;28:1667-1702.
- [52] Hong WI, Kim YH, Lee SW. An assumed strain triangular solid element with bubble function displacements for analysis of plates and shells. International Journal for Numerical Methods in Engineering 2001;52:455-469.
- [53] Ho SP, Yeh YL. The use of 2D enriched elements with bubble functions for finite element analysis. Computers and Structures 2006;84:2081-2091.
- [54] Jeon HM, Lee Y, Lee PS, Bathe KJ. The MITC3+ shell element in geometric nonlinear analysis. Computers and Structures, 2015;146:91-104.
- [55] Kim JH, Kim YH. A three-node  $C^0$  ANS element for geometrically non-linear structural analysis. Computer Methods in Applied Mechanics and Engineering 2002;191:4035-4059.
- [56] Leissa AW. Vibration of plates: NASA SP-160, 1969.
- [57] Leissa AW. Vibration of shells: NASA SP-288, 1973.
- [58] Leissa AW. The free vibration of rectangular plates. Journal of Sound and Vibration 1973;31:257-293.
- [59] Gorman DJ. Free vibration analysis of the completely free rectangular plate by the method of superposition. 1978;58:437-447.
- [60] Gorman DJ. Free vibration analysis of completely free rectangular plates by the superposition-Galerkin method. 2000;237:901-914.
- [61] Mochida Y, Ilanko S. Bounded natural frequencies of completely free rectangular plates. Journal of Sound and Vibration 2008;311:1-8.

[62] Hernandez E, Hervella-Nieto L, Rodriguez R. Computation of the vibration modes of plates and shells by low-order MITC quadrilateral finite elements. Computers and Structures 2003;81:615-628.

[63] Lee SJ. Free vibration analysis of plates by using a four-node finite element formulated with assumed natural transverse shear strain. Journal of Sound and Vibration 2004;278:657-684.

[64] Tan DY. Free vibration analysis of shells of revolution. Journal of Sound and Vibration 1998;213:15-33.

[65] MacNeal RH, Harder RL. A proposed standard set of problems to test finite element accuracy. Finite Element in Analysis and Design 1985;1:3-20.

[66] ANSYS Inc., ANSYS Tutorials 13.0; 2010.

[67] ABAQUS Inc., Abaqus Analysis User's Manual 6.12; 2012.

[68] Timoshenko SP, Woinowsky-Krieger S. Theory of Plates and Shells. Second Edition. New York: McGraw-Hill.

[69] Morley LSD. Skew Plates and Structures. Oxford: Pergamon Press; 1963.

[70] Ashwell DG, Sabir AB. A new cylindrical shell finite element based on simple independent strain functions. International Journal of Mechanics Sciences 1972;14:171-183.

[71] Sussman T and Bathe KJ. 3D-shell elements for structures in large strains. Computers and Structures 2013;122:2-12.

[72] Allman DJ. A compatible triangular element including vertex rotations for plane elasticity analysis. Computers and Structures 1984;19:1-8.

[73] Felippa CA. A study of optimal membrane triangles with drilling freedoms. Computer Methods in Applied Mechanics and Engineering 2003;192:2125-2168.

## 요약문

### 셀 구조물 해석을 위한 삼각형 유한요소의 개발

셀 구조물은 다양한 공학분야에서 많이 쓰이고 있으며, 지난 수십 년간 유한요소법은 셀 구조물 해석에 주요하게 쓰여 왔다. 효과적인 3절점 삼각형 셀 유한요소의 개발을 위해 많은 노력이 있었지만, 여전히 일반적인 셀 구조물 해석을 신뢰도 있고 효과적으로 하는 3절점 삼각형 셀 유한요소는 존재하지 않는다.

본 논문의 목적은 일반적인 셀 구조물 해석을 위한 효과적인 3절점 삼각형 셀 유한요소를 개발하는 것이다. 효과적인 3절점 셀 유한요소는 등방성(isotropy) 거동을 보이면서 정합성(consistency)과 타원율(ellipticity) 조건을 만족시키고 해의 수렴 성능 실험에서 셀 구조물의 형상, 두께, 경계조건, 작용하는 하중 등에 상관없이 최적의 수렴 성능을 보여야 한다.

개선된 성능을 보이는 3절점 MITC3-HR 삼각형 셀 유한요소가 개발되었다. Hellinger-Reissner 변분법 이론을 MITC(Mixed Interpolation of Tensorial Components)방법의 관점에서 수정을 하고, 새로운 근사전단변형률장(approximated transverse shear strain field)을 제안하였다. 개발된 MITC3-HR 셀 유한요소는 등방성(isotropy), 거짓영에너지모드(spurious zero energy mode), 조각(patch) 실험들을 포함한 기본적인 실험들을 모두 통과한다. 해의 수렴 성능 실험으로 진행된 4번의 완전히 구속된 정사각형 판 문제, 60도 기울어진 단순지지 판 문제, 원기둥(Cylinder) 문제, 쌍곡면(hyperboloid) 문제에서 MITC3-HR 셀 요소는 기존의 3절점 셀 유한요소인 MITC3 보다 개선된 성능을 나타내었다. 새로운 근사전단변형률장이 면내 뒤틀림(In-plane twisting) 모드를 약화시키면서 MITC3-HR 셀 요소의 성능을 개선시키는 것이다. 본 연구를 통하여 3절점 삼각형 셀 요소의 성능을 개선시키기 위해서는 면내 뒤틀림 모드를 약화시켜야 된다는 것을 알아내게 되었다.

효과적인 새로운 3절점 MITC3+ 삼각형 셀 요소가 개발되었다. 3차승을 가지는 베블함수를 굽힘 변위를 풍성하게 해주기 위하여 회전 자유도에 추가 되었다. 베블함수가 성능을 개선시킬 수 있게 작동하고, 면내 뒤틀림 모드(in-plane twisting mode)도 줄여서 전단잠김(shear locking)현상을 줄일 수 있는 새로운 표본선정기술(tying scheme)을 제시하였다. 이를 기반으로 새로운 대체전단변형률장(assumed transverse shear strain field)이 만들어졌다. MITC3+ 셀 유한요소는 등방성(isotropy), 거짓영에너지모드(spurious zero energy mode), 조각(patch)실험들을 포함한 기본적인 실험들을 모두 통과하며, 다양한 판과 셀 구조물의 검증문제(benchmark problems)에서 해의 수렴성능이 우수하였다. 또한, 판과 셀 구조물의 검증문제에서 요소망이 찌그러진 것을 사용하여도 MITC3+ 셀 요소는 여전히 우수한 성능을 보여 주었다.

개발된 MITC3+ 셀 요소는 다양한 선형 및 기하학적 비선형 정적 해석문제에서 우수한 성능을 보인다. 그래서 정적 및 동적인 모드해석을 통하여 MITC3+ 셀 요소의 기본 메커니즘과 특성에 대한 통찰력을 얻는 연구를 하였다. 정적모드 해석을 위해서는 하나의 직각 삼각형과 두 개의 직각 삼각형의 결합으로 이루어진 직각 사각형을 각각 이용하였다. 각 굽힘 모드에 대한 변형률장이 구해졌으며, 전단잠김 현상이 모드수준에서 어떻게 줄어드는지 밝혀 낼 수 있었다. 또한, 기존의 3절점 셀 요소(MITC3)를 사용하였을 때 잠김현상이 일어나는 두 개 변이 구속된 정사각형 판 구조물 문제에서 MITC3+ 셀 요소가 순수굽힘조건을 잘 나타낸다는 것을 해석적으로 밝혔다. 셀 구조물의 동적모드해석에서는 MITC3+ 셀 요소는 요소망의 찌그러짐에 상관 없이 우수한 성능을 보여 주었다.

핵심어: 셀 구조물; 셀 유한요소; 3절점 요소; MITC 방법; 수렴성

